DISSERTATIONES
PHYSICAE
UNIVERSITATIS
TARTUENSIS
144

ALEKSEI KUBARSKI

Dynamical symmetry breaking and dark matter

DISSERTATIONES PHYSICAE UNIVERSITATIS TARTUENSIS
144

DISSERTATIONES PHYSICAE UNIVERSITATIS TARTUENSIS
144

ALEKSEI KUBARSKI

Dynamical symmetry breaking and dark matter

UNIVERSITY OF TARTU
Press
1632

This study was carried out at the National Institute of Chemical Physics and Biophysics, Tallinn, and at the University of Tartu, Estonia.

The dissertation was admitted on 13.05.2026 in partial fulfillment of the requirements for the degree of Doctor of Philosophy in physics, and was allowed for defence by the Council of the Institute of Physics, University of Tartu.

Supervisors: Dr. Kristjan Kannike,
National Institute of Chemical Physics and Biophysics,
Tallinn, Estonia

Dr. Luca Marzola,
National Institute of Chemical Physics and Biophysics,
Tallinn, Estonia

Dr. Laur Järv,
University of Tartu,
Tartu, Estonia

Opponent: Prof. Oleg Lebedev
University of Helsinki,
Helsinki, Finland

Defence: June 17, 2026, University of Tartu, Estonia

ISSN 1406-0647 (print)
ISBN 978-9908-57-229-1 (print)
ISSN 2806-2523 (pdf)
ISBN 978-9908-57-230-7 (pdf)

University of Tartu Press
www.tyk.ee

Contents

List of original publications

The results of this Thesis are compiled in the three following research publications:

I. K. Kannike, A. Kubarski and L. Marzola, "Geometry of Flat Directions in Scale-Invariant Potentials," Phys. Rev. D **99** (2019) no.11, 115034 doi:10.1103/PhysRevD.99.115034, arXiv:1904.07867 [hep-ph].

II. K. Kannike, N. Koivunen, A. Kubarski, L. Marzola, M. Raidal, A. Strumia and V. Vipp, "Dark matter-induced multi-phase dynamical symmetry breaking," Phys. Lett. B **832** (2022), 137214 doi:10.1016/j.physletb.2022.137214, arXiv:2204.01744 [hep-ph].

III. K. Kannike, A. Kubarski, L. Marzola and A. Racioppi, "Pseudo-Goldstone dark matter in a radiative inverse seesaw scenario," JHEP **12** (2023), 166 doi:10.1007/JHEP12(2023)166, arXiv:2306.07865 [hep-ph].

Author's contribution

In Publication I, the dissertant performed the analytical derivation for the biquadratic case and cross-checked the results for the general potential, as well as computed illustrative examples for both cases. The dissertant also contributed to the writing of the manuscript together with the co-authors.

In Publication II, the dissertant performed the phenomenological analysis of the model, contributing primarily to the calculation of the dark matter direct detection rate and the perturbativity scale of the model, and prepared the corresponding figures. The dissertant also contributed to the writing of the manuscript together with the co-authors.

In Publication III, the dissertant was a leading author and carried out the majority of the work. He took an active part in the discussions that led to the development of the theoretical framework and coordinated the contributions of the other authors. The dissertant established the parametrization of the model, performed the phenomenological analysis, and developed a Monte Carlo simulation code to explore its parameter space. Except for the inflationary part of the paper, the dissertant carried out all analytical and numerical computations, including the preparation of tables and figures. The dissertant also made the most substantial contribution to the writing of the manuscript.

Other publications of the dissertant

I. K. Kannike, A. Kubarski, L. Marzola and A. Racioppi, "A minimal model of inflation and dark radiation," Phys. Lett. B **792** (2019), 74-80 doi:10.1016/j.physletb.2019.03.025, arXiv:1810.12689 [hep-ph].

II. K. Kannike, N. Koivunen and A. Kubarski, "Is our vacuum global in a 331 model with three triplets?," JHEP **01** (2026), 115 doi:10.1007/JHEP01(2026)115 arXiv:2509.18250 [hep-ph].

Acknowledgments

I would like to thank my supervisors. Kristjan Kannike has been my supervisor since the very beginning of my research career—already from my undergraduate studies, about ten years ago. It is fair to say that his influence has been immense in shaping my scientific thinking, techniques, and development as a researcher. He has always been ready to answer my questions and help me solve research-related problems, even on weekends and outside regular working hours. I am grateful to Luca Marzola for his straightforwardness and for always encouraging me to broaden my knowledge and to double-check other people's work. Finally, I thank Laur Järv for his help with administrative matters and for fostering a friendly and supportive working atmosphere.

I would also like to thank the co-authors of my papers. I have collaborated with Antonio Racioppi on multiple projects, and he has always been a pleasure to work with. I am fascinated by Alessandro Strumia's ideas and proud to have had the opportunity to work with him. It has also been a great pleasure to collaborate with Niko Koivunen, Martti Raidal, and Venno Vipp, whose informal attitude and openness to discussion made our work together both productive and enjoyable.

I cannot stress enough how grateful I am to the National Institute of Chemical Physics and Biophysics, and in particular to the High Energy and Computational Physics research group, for welcoming me as one of their own and for providing financial support that allowed me to focus on the work I love while maintaining a comfortable life for myself and my family. I would also like to acknowledge the Estonian Research Council and the Ministry of Education and Research, whose grants PRG1677, RVTT3, TEM-TA23, and TK202 directly supported my research.

Finally, I wish to express my deepest gratitude to my family, especially to my wife Katriin. I may sometimes take her support for granted, but I am truly fortunate to be able to rely on her, even throughout this difficult year that has been marked by one personal tragedy after another. I also thank my children, Theadora, Irene, and Gaius, whose joy and laughter never fail to lift my spirits. Lastly, I dedicate this work, the result of years of effort, to my first son, who, sadly, left this world before birth.

Chapter 1

Introduction

The Standard Model of particle physics, formulated in the 1970s [1–3], has been an extremely successful theory in describing the elementary particles and the fundamental interactions between them, apart from gravity. The last particle predicted by the model, the Higgs boson, was discovered in 2012 [4, 5], marking another great success that demonstrated the internal consistency and predictive power of the model. Despite these achievements, the Standard Model remains an incomplete description of nature, and many open questions in particle physics still await answers.

The most weakly interacting particles in the Standard Model, neutrinos, are assumed to be massless. Neutrino oscillation experiments, however, have firmly established that at least two of the three generations possess nonzero masses [6–8]. Introducing right-handed neutrinos allows one to add a mass term in analogy with other fermions by tuning the corresponding Yukawa couplings. Such an approach, though, further exacerbates the already large hierarchy of Higgs couplings and is therefore unsatisfactory. A more elaborate mechanism is thus preferred.

Current experimental data strongly suggest that the electroweak vacuum of the Standard Model is metastable [9]. Given the present particle content, this vacuum remains highly long-lived and metastable, thereby not yielding an immediate problem as tunneling to the true vacuum remains exceedingly unlikely. Nevertheless, many find the metastability of our vacuum state conceptually unsatisfactory. Moreover, issues may arise when extending the Standard Model with particles which can further destabilize the vacuum—for example by introducing new heavy fermions, as is often done in neutrino mass generation models.

From a cosmological perspective, great success has been achieved by the standard model of cosmology, the ΛCDM model [10], which postulates the existence of dark energy and dark matter as the dominant components of the energy budget of the universe. However, it does not explain the nature

of either. The latter—dark matter—is essential for explaining large-scale structure formation [11–13], the rotational velocities of stars around galactic centers [14, 15], and the acoustic peaks of the cosmic microwave background [16]. Although there is an active community exploring explanations of dark matter within the framework of modified gravity, a particle physics interpretation is often considered more natural, as it consistently fits observations across multiple scales. This, however, necessitates going beyond the Standard Model, which contains no viable dark matter candidate.

Another widely accepted paradigm in cosmology is inflation [17–19]—a period of rapid accelerated expansion in the very early universe. Inflation provides elegant solutions to the horizon and flatness problems [18] and can be driven by the false vacuum of a scalar field potential. In principle, the Higgs boson, as the only scalar field of the Standard Model, could serve as the inflaton whose potential drives inflation. However, alternative possibilities arise naturally in models with an extended scalar sector, and these must also be explored.

Finally, the Standard Model contains exactly one dimensionful parameter: the Higgs mass term. This is not only aesthetically unappealing but also gives rise to the possible naturalness problem. The Higgs mass receives large quantum corrections proportional to the scale of new physics, requiring delicate fine-tuning of the bare mass to cancel these contributions [20]. Motivated by this issue, this thesis explores the framework of classically scale-invariant models, which eliminate problematic dimensionful terms from the potential. However, this framework is experimentally excluded within the Standard Model itself: therefore extensions of the scalar sector with new particles such as the dilaton and, possibly, scalar dark matter candidates are necessary. The introduction of new degrees of freedom, in turn, provides an excellent opportunity to also investigate other open questions of both the Standard Model and cosmology.

This thesis is structured as follows. Chapter 2 provides a brief overview of the Standard Model of particle physics, with a focus on the Higgs boson, the hierarchy problem, and the issue of vacuum metastability. In Chapter 3, the discussion shifts to cosmology, where a concise overview of the history of the universe is given. We examine the standard cosmological model known as the ΛCDM model, describe the properties of dark matter most relevant for this work—including its production and detection—and introduce the concept of cosmic inflation. Chapter 4 presents the experimental evidence for neutrino masses and discusses possible mechanisms for their generation. In Chapter 5, we explain the essence of classically scale-invariant models and present novel approaches to their analysis, illustrated through two concrete models. Finally, the summary are provided in Chapter 6 and Chapter 7, in English and Estonian, respectively.

Chapter 2

Standard model of particle physics

The Standard Model of particle physics is a relativistic quantum field theory [21] that describes all known elementary particles and the fundamental interactions between them: the electromagnetic, weak, and strong forces [22–25]. The theory of quantum gravity remains unknown and is therefore excluded. Fortunately, gravitational interactions are negligible at particle physics energy scales and do not affect the discussion that follows. Electromagnetic and weak interactions among leptons and quarks are described by a Yang–Mills theory [26], based on the symmetry group $SU(2)_L \times U(1)_Y$ before symmetry breaking (see section 2.1). Here, the subscript Y refers to hypercharge, while L denotes left-handed fields that transform as doublets under $SU(2)_L$, associated with the weak isospin quantum number. Strong interactions among quarks are based on the symmetry group $SU(3)_C$, with the subscript referring to the colour quantum number, and are described by the gauge theory of quantum chromodynamics [23].

Each symmetry group is associated with gauge fields, whose spin-one bosons mediate the corresponding interactions. For the $U(1)_Y$ generator, the associated field is B_μ, for the $SU(2)_L$ the three generators t^a (with $a = 1, 2, 3$) correspond to the gauge fields W_μ^a and for $SU(3)_C$ there is an octet of gluon fields G_μ^α (with $\alpha = 1, 2, .., 8$) for eight T^α generators. These generators satisfy the following relations:

$$\begin{aligned} [t^a, t^b] &= i\varepsilon^{abc} t_c, \\ [T^\alpha, T^\beta] &= i f^{\alpha\beta\gamma} T_\gamma, \\ \mathrm{Tr}(T^\alpha T^\beta) &= \frac{1}{2}\delta^{\alpha\beta}, \end{aligned} \tag{2.1}$$

where ε^{abc} is the antisymmetric Levi-Civita symbol, and $f^{\alpha\beta\gamma}$ are the structure constants of $SU(3)_C$. The generators of $SU(2)_L$ are typically expressed

as $t^a = \sigma^i/2$, where σ^i are Pauli matrices, while those of $SU(3)_C$ are given by $T^\alpha = \lambda^\alpha/2$, with λ^α being the Gell-Mann matrices. The field strength tensors of the gauge fields are given by:

$$\begin{aligned} G^\alpha_{\mu\nu} &= \partial_\mu G^\alpha_\nu - \partial_\nu G^\alpha_\mu + g_s f^{\alpha\beta\gamma} G^\beta_\mu G^\gamma_\nu, \\ W^a_{\mu\nu} &= \partial_\mu W^a_\nu - \partial_\nu W^a_\mu + g_2 f^{abc} W^b_\mu W^c_\nu, \\ B_{\mu\nu} &= \partial_\mu B_\nu - \partial_\nu B_\mu. \end{aligned} \tag{2.2}$$

Here, g_s and g_2 are the coupling constants of the strong and weak interactions, respectively. The hypercharge coupling g_1 is not present in the expression of the related field strength as gauge fields associated to Abelian groups do not have self-interactions. The Lagrangian of the Standard Model must remain invariant under local gauge transformations, meaning that the theory must be independent of arbitrary local choices of phase or gauge basis. As a simple example, under a local $U(1)$ symmetry the field transforms as

$$\psi(x) \to e^{i\alpha(x)}\psi(x). \tag{2.3}$$

It is easy to see that this invariance is broken by a kinetic term involving only ordinary spacetime derivatives. To ensure invariance under such transformations, one must instead use the covariant derivative:

$$D_\mu = \partial_\mu - i g_s T_a G^a_\mu - i g_2 t_a W^a_\mu - i g_1 \frac{Y}{2} B_\mu. \tag{2.4}$$

The fermions have half-integer spin and are described by spinor fields. There are three generations of fermions with the same quantum numbers and gauge representations but different masses, as shown in Table 2.1. Finally, the Standard Model also includes a single spin-zero boson field, called the Higgs field, which transforms as an $SU(2)_L$ doublet with hypercharge $Y = 1$, and as singlet under the $SU(3)_C$ group. With this field content, one can construct the following renormalizable, gauge-invariant Lagrangian:

$$\begin{aligned} \mathcal{L}_{\text{SM}} = &-\frac{1}{4} G^a_{\mu\nu} G^{\mu\nu}_a - \frac{1}{4} W^a_{\mu\nu} W^{\mu\nu}_a - \frac{1}{4} B_{\mu\nu} B^{\mu\nu} \\ &+ \bar{L} \not{D} L + \bar{e}_R \not{D} e_R + \bar{Q} \not{D} Q + \bar{u}_R \not{D} u_R + \bar{d}_R \not{D} d_R \\ &+ (D^\mu H)^\dagger (D_\mu H) - V(H) \\ &- Y_e \bar{L} H e_R - Y_d \bar{Q} H d_R - Y_u \bar{Q} \tilde{H} u_R + \text{h. c}, \end{aligned} \tag{2.5}$$

where we have omitted generation indices. The fermion content are summarized in the table 2.1. The quantity $\not{D} = D_\mu \gamma^\mu$ denotes the covariant derivative contracted with the Dirac matrices, and $\tilde{H} = i\tau_2 H^*$ is the isospin conjugate of the Higgs doublet H. The first line in the Lagrangian describes the dynamics and self-interactions of the gauge bosons. The second line contains

Table 2.1: Fermion content of the Standard Model, including their hypercharge and representation under the gauge groups. Generation indices are omitted for clearness. Note that right-handed leptons do not include neutrinos.

Name	Symbol	Y	$SU(2)_L$	$SU(3)_C$
Left-handed leptons	$L_L = (e_L, \nu_L)^T$	-1	2	1
Left-handed quarks	$Q_L = (u_L, d_L)^T$	$\frac{1}{3}$	2	3
Right-handed leptons	e_R	-2	1	1
Right-handed u-type quarks	u_R	$\frac{4}{3}$	1	3
Right-handed d-type quarks	d_R	$-\frac{2}{3}$	1	3

the kinetic terms of the fermions. Note that due to the covariant derivative, these terms also describe their interactions with gauge bosons. The third line describes the kinetic term and potential of the Higgs field given by equation (2.7). Finally, the last line contains the Yukawa interactions between the Higgs boson and fermions. In the electroweak sector of the theory, no explicit fermion mass terms can be added because left-handed fermions are $SU(2)_L$ doublets and right-handed fermions are singlets. Nevertheless, the Higgs potential provides a source of spontaneous symmetry breaking via the Higgs–Brout–Englert–Guralnik–Hagen–Kibble mechanism [27–31], or the Higgs mechanism for short, which is discussed in the next section.

2.1 Higgs boson and spontaneous symmetry breaking

The scalar sector of the Standard Model consists of a single field, the Higgs boson, as described above. As a complex $SU(2)_L$ doublet, it can be written as

$$H = \begin{pmatrix} h^+ \\ h^0 \end{pmatrix}, \tag{2.6}$$

with one electrically charged component and one neutral component. The scalar potential in the Lagrangian (2.5) is given by

$$V(H) = \mu_h^2 H^\dagger H + \lambda_h (H^\dagger H)^2. \tag{2.7}$$

In the case of $\mu_h^2 < 0$ and $\lambda_h > 0$, this potential has a minimum away from the origin of the coordinates. After symmetry breaking, the $U(1)_{\mathrm{EM}}$ subgroup remains unbroken, corresponding to electromagnetism, with the associated gauge field identified as the photon, which therefore remains massless. Consequently, only the neutral component of the Higgs field

acquires a vacuum expectation value (VEV):

$$\langle 0|H|0\rangle = \begin{pmatrix} 0 \\ \frac{v_h}{\sqrt{2}} \end{pmatrix} \tag{2.8}$$

with $v_h = \sqrt{-\mu_h^2/\lambda_h}$. It is convenient to rewrite the Higgs doublet as

$$H(x) = \begin{pmatrix} \theta_1 + i\theta_2 \\ \frac{v_h+h}{\sqrt{2}} + i\theta_3 \end{pmatrix} = e^{i\pi_a(x)t^a} \begin{pmatrix} 0 \\ \frac{v_h+h(x)}{\sqrt{2}} \end{pmatrix}, \tag{2.9}$$

with fields $\pi_a(x)$ related to Goldstone bosons θ_a appearing in the linear parametrisation. This can be simplified with a gauge transformation to the unitary gauge:

$$H(x) \to e^{-i\pi_a(x)t^a} H(x) = \begin{pmatrix} 0 \\ \frac{v_h+h(x)}{\sqrt{2}} \end{pmatrix}. \tag{2.10}$$

After expanding the Higgs kinetic term in the Lagrangian, one gets following terms:

$$\mathcal{L}_{\text{SM}} = \frac{1}{8} g_2^2 v_h^2 \left|W_\mu^1 + iW_\mu^2\right|^2 + \frac{1}{8} v_h^2 \left(g_2 W_\mu^3 - g_1 B_\mu\right)^2 + ..., \tag{2.11}$$

which are mass terms for the gauge bosons. By redefining the gauge fields as

$$W_\mu^\pm = \frac{1}{\sqrt{2}} \left(W_\mu^1 \mp iW_\mu^2\right), \; Z_\mu = \frac{g_2 W_\mu^3 - g_1 B_\mu}{\sqrt{g_1^2 + g_2^2}}, \; A_\mu = \frac{g_2 W_\mu^3 + g_1 B_\mu}{\sqrt{g_1^2 + g_2^2}}, \tag{2.12}$$

the corresponding gauge boson masses are

$$M_W = \frac{g_2 v_h}{2}, \quad M_Z = \frac{\sqrt{g_1^2 + g_2^2}}{2} v_h. \tag{2.13}$$

The photon field A_μ remains massless. The three degrees of freedom θ_i, called Goldstone bosons, initially present in Eq. (2.9), are absorbed by the three massive gauge bosons [32], providing them with their longitudinal components. The non-zero VEV spontaneously breaks the symmetry $SU(2)_L \times U(1)_Y \to U(1)_{\text{EM}}$, leaving a residual $U(1)_{\text{EM}}$ symmetry associated with the electromagnetic interaction and the photon field. The associated conserved quantum number, the electric charge Q, is related to the hypercharge Y and the diagonal generator t_3 of $SU(2)_L$, corresponding to the weak isospin, as

$$Q = t_3 + \frac{Y}{2}. \tag{2.14}$$

Fermions acquire mass after symmetry breaking through Yukawa interactions with the Higgs boson, with the mass given by

$$m_f = \frac{y_f v_h}{\sqrt{2}}, \tag{2.15}$$

where m_f is the fermion mass and y_f is the Yukawa coupling of the fermion to the Higgs boson. Finally, the physical Higgs boson mass is given by

$$m_h^2 = 2\lambda_h v_h^2. \tag{2.16}$$

Great effort has been devoted to determining the VEV of the Higgs boson, v_h. The most precise determination comes from measurements of the muon lifetime and mass, which can be expressed as

$$\tau_\mu = \frac{1536\hbar\pi^3}{C_W^2 m_\mu^5}, \tag{2.17}$$

where m_μ is muon mass and C_W is the Wilson coefficient, which can be determined from experimental data on the muon lifetime and mass. In the Standard Model, muon decays are mediated by the W boson, and the Wilson coefficient can be related to Standard Model parameters as

$$C_W = -\frac{g_2^2}{2M_W^2} = -2\frac{1}{v_h^2} \rightarrow v_h = \sqrt{\frac{2}{|C_W|}}. \tag{2.18}$$

Using the experimental values of the muon lifetime, $\tau_\mu = 2.1969811(22)\mu$s, and its mass, $m_\mu = 105.6583745(24)$MeV [33], the resulting value of the Higgs VEV is

$$v_h = 246.21964(6)\text{GeV}. \tag{2.19}$$

With the VEV determined, one can obtain the couplings of the Higgs boson by measuring the masses of the corresponding particles.

2.1.1 Naturalness of the electroweak scale

In quantum field theory, classical (tree-level) parameters receive quantum corrections from loop diagrams. Unlike other fields in the Standard Model, the Higgs boson is not protected against large corrections by any symmetry, such as chiral symmetry for fermions or gauge invariance for gauge bosons [20]. As a consequence, the Higgs boson mass receives quadratically divergent corrections proportional to some new physics cut-off scale Λ. Explicitly, the one-loop correction can be approximated by

$$\delta m_h^2 = \frac{\Lambda^2}{32\pi^2}\left(6\lambda_h + \frac{1}{4}(3g_1^2 + 9g_2^2) - y_t^2\right), \tag{2.20}$$

which includes the most relevant contributions. The Standard Model is typically assumed to be valid up to the Planck scale, $\sim 10^{19}$ GeV. This cut-off scale Λ may correspond to any new physics between the electroweak scale (around $\sim$ 100 GeV) and the Planck scale. The combined experimental measurement of the Higgs boson mass is provided by [34] and is

$$m_h = 125.11 \pm 0.11\text{GeV}. \tag{2.21}$$

For the Higgs boson mass to remain so small compared to the potential scale of new physics, the tree-level mass must be fine-tuned to cancel out large quantum corrections. The quadratic sensitivity of the Higgs boson mass, and the resulting unnatural fine-tuning of the tree-level parameter, is known as the hierarchy problem. The hierarchy problem is independent of the chosen renormalization scheme, and it persists even if new physics couples to the Higgs boson indirectly, as long as it interacts with the Standard Model [35]. A possible solution to the hierarchy problem is described in the Chapter 5 in the context of classically scale-invariant models.

2.1.2 Metastability of electroweak vacuum

At very high energy scales, the Higgs potential is dominated by the quartic term:

$$V(h \gg m_t) \approx \frac{1}{4}\lambda_h h^4. \tag{2.22}$$

In quantum field theory, couplings are not constant but run with renormalization scale μ instead [3, 36, 37]. If at any scale λ_h becomes negative, the potential acquires a new, much deeper minimum, rendering the electroweak vacuum we inhabit unstable. The dominant one-loop contribution to the β-function describing the evolution of λ_h is

$$\begin{aligned}\beta_{\lambda_h} = \frac{d\lambda_h}{d\ln\mu} = \frac{1}{16\pi^2}\Bigg(&-6y_t^4 + 12y_t^2\lambda_h + \frac{3}{8}\left(2g_2^4 + \left(g_1^2+g_2^2\right)^2\right) \\ &- 3\lambda_h\left(3g_2^2+g_1^2\right) + 24\lambda_h^2\Bigg).\end{aligned} \tag{2.23}$$

The beta-function β_{λ_h} depends on the fourth power of the top-quark Yukawa coupling y_t, which is determined experimentally from top-quark mass measurements [38]. Its value at low energy is

$$y_t = \frac{\sqrt{2}m_t}{v_h} = \frac{\sqrt{2}\cdot 172.52\text{GeV}}{246.22\text{GeV}} = 0.99090, \tag{2.24}$$

making the quartic top Yukawa term in (2.23) the largest contribution. This drives λ_h to negative values at around the scale $\mu \simeq 10^{10}$ GeV, as shown in

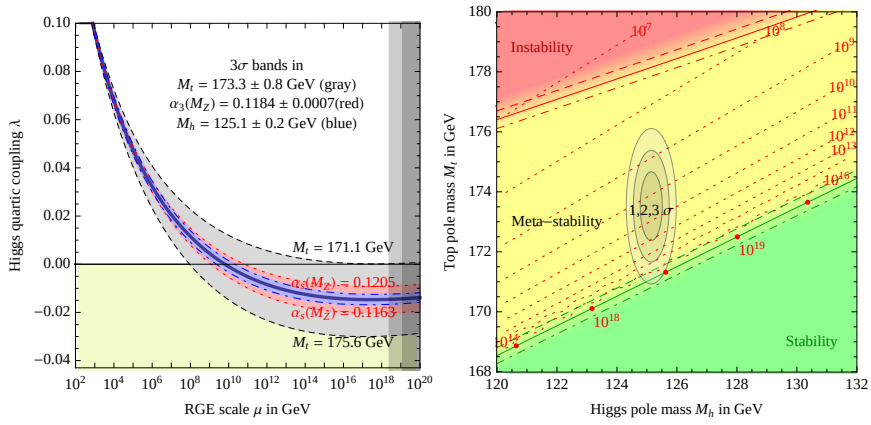

Figure 2.1: Left: Running of the Higgs quartic coupling λ_h. Right: Regions of stability (green), metastability (yellow), and instability (red) of the electroweak vacuum in the plane of top-quark and Higgs boson masses. Plots are taken from [9].

the right panel of Figure 2.1. The left panel shows that, despite the existence of a deeper minimum, we inhabit a metastable vacuum. To clarify the meaning of metastability, one must calculate the probability of quantum tunneling to the true vacuum. This can be done using semi-classical methods [39]. The probability $d\wp$ of nucleating a bubble of true vacuum within a spatial volume dV and time interval dt can be calculated as

$$d\wp = \Lambda_B^4 e^{-S(\Lambda_B)} dV dt, \tag{2.25}$$

where Λ_B is the characteristic scale at which the decay is most likely to occur. It can be chosen to maximize the expression $\Lambda_B^4 e^{-S(\Lambda_B)}$, which roughly corresponds to the region where $\beta_{\lambda_h}(\Lambda_B) = 0$. Following the derivation in [9], a simple analytical approximation of the action is obtained using the four-dimensional Euclidean tunneling bounce solution:

$$S(\Lambda_B) = S_4(\Lambda_B) = \frac{8\pi^2}{3|\lambda_h(\Lambda_B)|}. \tag{2.26}$$

The total probability that a bubble of true vacuum has nucleated during the history of the universe is

$$\wp = \Lambda_B^4 e^{-S(\Lambda_B)} \int_0^{t_0} dt \int_{|x|<a(\eta_0-\eta)} d^3x \approx 0.15 \frac{\Lambda_B^4}{H_0^4} e^{-S(\Lambda_B)} \tag{2.27}$$

where the final expression provides a rough estimate of the integral, as derived in [9]. Here, $H_0 = 66.7$km/s/Mpc [40] is the present-day Hubble rate, further discussed in Chapter 3. Using this expression, one can estimate the probability of electroweak vacuum decay to be less than 10^{-1000},

making such a decay extremely unlikely. This renders the electroweak vacuum metastable, in agreement with current observations. Nevertheless, if one considers models beyond the Standard Model, the stability of the electroweak vacuum must be revisited. For example, the addition of extra scalar fields can contribute positively to β_{λ_h}, potentially resulting in a more satisfactory, fully stable electroweak vacuum, as will be discussed later in this thesis.

Chapter 3

Cosmology

New developments in 20th-century astronomical observations, together with the mathematical framework provided by General Relativity [41, 42], led to the emergence of modern cosmology. A cornerstone of this field is the discovery of the expanding universe by Georges Lemaître [43] and Edwin Hubble [44], which culminated in what is now known as the Hubble–Lemaître law, a fundamental relation in cosmology:

$$\dot{\vec{r}} = H(t)\vec{r}, \tag{3.1}$$

where $H(t) > 0$ is the Hubble rate (or Hubble parameter), whose present-day value is observed to be $66.7\ \mathrm{km\,s^{-1}\,Mpc^{-1}}$ [40] and r denotes the distance between two objects in space. Under general assumptions in cosmology, the Einstein equations of General Relativity lead to a mathematical singularity at a finite scale, known historically as the Big Bang singularity. This is outlined in Section 3.1, where the standard model of cosmology—the so-called ΛCDM model—is introduced. Beyond this point, General Relativity breaks down, and we currently lack both the mathematical tools and physical understanding to describe the very early universe. Moreover, the Big Bang model leaves several open problems, most notably the flatness problem and the horizon problem. In Section 3.2, we discuss the most widely accepted solution to these problems: cosmic inflation.

This chapter provides only a brief review of the evolution of the universe, focusing particularly on its early stages and current energy content. It closely follows more detailed reviews on cosmic inflation [45–48] and dark matter [49].

3.1 ΛCDM model

Arguably the most important observational data on the early universe comes from the cosmic microwave background (CMB), which offers a snapshot of

the universe when it became transparent to photons during the matter-dominated epoch, at a redshift of approximately $z \simeq 1100$ (about 380,000 years after the Big Bang). The most precise CMB measurements have been provided by the Planck satellite [16], which is major success in the confirmation of the cosmological principle, which states that the universe is isotropic and homogeneous on large scales. The Planck results show that the CMB is statistically consistent with this symmetry on scales larger than roughly 100 Mpc.

Using the cosmological principle, the most general metric that can be constructed is the Friedmann–Robertson–Walker (FRW) metric:

$$ds^2 = -dt^2 + a^2(t)\left(\frac{dr^2}{1-kr^2} + r^2(d\theta^2 + \sin^2\theta d\phi^2)\right), \tag{3.2}$$

where $a(t)$ is the scale factor, which evolves with time and encodes the expansion of the universe. The coordinates r, θ, ϕ are comoving spherical coordinates, meaning they remain fixed for observers who are at rest with respect to the overall expansion of the universe. The constant k determines the spatial curvature of the universe, with possible values:

- $k = 1$: a closed universe, corresponding to a 3-sphere,
- $k = -1$: an open universe, corresponding to a hyperbolic geometry,
- $k = 0$: a flat universe, corresponding to Euclidean space.

The relative rate of expansion of the universe is described by the previously introduced Hubble parameter, which relates to the scale factor $a(t)$ as

$$H = \frac{\dot{a}}{a}, \tag{3.3}$$

where the explicit time dependence is omitted here and throughout this chapter for simplicity. One studies the evolution of the scale factor on a homogenous and isotropic background by solving the Einstein field equations, which relate the Einstein tensor to the energy–momentum tensor:

$$G_{\mu\nu} + \Lambda g_{\mu\nu} = \frac{T_{\mu\nu}}{M_P^2}, \tag{3.4}$$

where Λ denotes the vacuum energy, commonly referred to as the cosmological constant or dark energy. If the energy–momentum content of the universe is modeled as a perfect fluid, it can be written as

$$T^{\mu}_{\nu} = \mathrm{Diag}(-\rho, p, p, p), \tag{3.5}$$

Table 3.1: Constituents of the universe with their equation-of-state parameter w, energy density scaling with the scale factor, and scale factor evolution assuming each component dominates. Present-day densities $\Omega_{i,0}$ are based on Planck measurements [16], consistent with a flat universe.

	w	$\rho \propto$	$a \propto$	$\Omega_{i,0}$
Radiation	$\frac{1}{3}$	a^{-4}	$t^{1/2}$	$\sim 10^{-5}$
Baryonic matter	0	a^{-3}	$t^{2/3}$	0.049
Dark matter	0	a^{-3}	$t^{2/3}$	0.266
Curvature	$-\frac{1}{3}$	a^{-2}	t^{1}	0.0004
Λ	-1	a^{0}	e^{Ht}	0.685

with energy density ρ and pressure p. By substituting the FRW metric into the Einstein tensor defined as

$$G_{\mu\nu} = R_{\mu\nu} - \frac{1}{2}Rg_{\mu\nu}, \tag{3.6}$$

one arrives at the Friedmann equations:

$$\begin{aligned} H^2 &= \left(\frac{\dot{a}}{a}\right)^2 = \frac{\rho}{3M_P^2} - \frac{k}{a^2} + \frac{\Lambda}{3}, \\ \dot{H} + H^2 &= \frac{\ddot{a}}{a} = -\frac{1}{6M_P^2}(\rho + 3p) + \frac{\Lambda}{3}. \end{aligned} \tag{3.7}$$

Combining these two equations will give rise to differential continuity equation

$$\frac{d\rho}{dt} + 3H(\rho + p) = 0. \tag{3.8}$$

This equation describes the dilution of energy density during the expansion of the universe. Its solution is

$$\rho \propto a^{-3(1+w)}, \tag{3.9}$$

where $w = p/\rho$ is the equation-of-state parameter, which depends on the specific component of the universe. Different constituents and their corresponding values of w, along with their dilution behavior as a function of the scale factor, are listed in Table 3.1. According to the ΛCDM model, the universe consists not only of baryonic matter and radiation, but also of the previously introduced cosmological constant Λ, and non-relativistic, non-interacting matter known as dark matter [50], which will be discussed further in Subsection 3.1.1. This framework is in excellent agreement with observations and is therefore regarded as the current standard model of Big Bang cosmology.

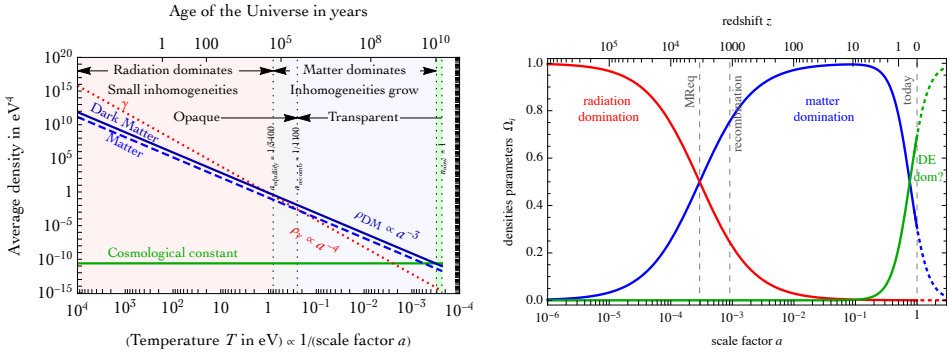

Figure 3.1: Evolution of the energy densities of the components of the universe. The plots are taken from [49].

By combining Eq. (3.9) with the Friedmann Eqs. (3.7), one obtains the time evolution of the scale factor for different dominant energy components:

$$a \propto \begin{cases} t^{\frac{2}{3}(1+w)}, & w \neq -1 \\ e^{Ht}, & w = -1 \end{cases} \tag{3.10}$$

Due to the differing rates of dilution, different components dominate the energy budget of the universe at different times—beginning with radiation-dominated epochs, followed by matter domination, and eventually entering a phase dominated by the cosmological constant, whose energy density remains constant during expansion. This evolution is illustrated in Figure 3.1.

It is convenient to express present time energy densities of the universe's components as fractions of the critical density, defined by $\rho_c = 3M_P^2H^2$, which corresponds to a spatially flat universe. Each component's density parameter is then given by $\Omega_{i,0} = \rho_i/\rho_c$. Using this, the Friedmann equation can be rewritten as

$$\left(\frac{H}{H_0}\right)^2 = \sum_i \Omega_{i,0} a^{-3(1+w_i)} + \Omega_{k,0} a^{-2} \tag{3.11}$$

where we have set $a_0 = 1$, and written the curvature contribution $\Omega_{k,0}$ explicitly outside the sum to better illustrate the consistency condition

$$\sum_i \Omega_{i,0} + \Omega_{k,0} = 1. \tag{3.12}$$

The observed values of $\Omega_{i,0}$ are presented in the last column of Table 3.1. As shown in the table, today's energy budget of the universe consists of only about 5% of baryonic matter and a negligible contribution from radiation. The remaining 95% is divided between dark matter and dark energy, under

the assumption that dark energy is indeed a cosmological constant. Measurements of the CMB, combined with large-scale structure observations, are consistent with a flat universe, constraining the curvature parameter to $\Omega_{k,0} = 0.0004(18)$ [41].

3.1.1 Dark matter

Measurements of the CMB acoustic peaks [16], together with simulations of nonlinear growth of primordial inhomogeneities and the formation of large-scale structures [11–13], indicate the presence of an additional component of the universe with the same equation of state as baryonic matter but with negligible non-gravitational interactions. In particular, its lack of interaction with the electromagnetic force led to the name dark matter.

Apart from fitting extremely well with the observations mentioned above, dark matter also explains a variety of observables on very different scales, such as the rotation curves of spiral galaxies [14, 15], colliding clusters [51], and cosmic shear [52, 53]. Its impact across such a wide range, from individual galaxies to the entire observable universe, makes a yet-to-be-discovered particle (or particles) one of the most natural explanation. Although all current observations rely only on the gravitational effects of dark matter, and any non-gravitational interactions must be negligible on astrophysical scales, this does not exclude the possibility of interactions with the Standard Model content. In fact, most models of dark matter generation assume some level of interaction with ordinary matter, and numerous experiments have been conducted, and continue to be conducted, to detect dark matter through its possible couplings to the Standard Model content.

Properties from cosmological observations

To effectively assist in the formation of large-scale structures, dark matter must be non-relativistic at the onset of structure formation and in all subsequent epochs [54]. This requirement is emphasized in the ΛCDM model through the designation “cold” dark matter. Otherwise, fast-moving dark matter particles would suppress the growth of perturbations in a manner similar to the photon–baryon fluid before recombination. This cold dark matter bound usually translates into model depending bounds on dark matter mass and interactions with relativistic particles.

Observations such as colliding galaxy clusters also place bounds on dark matter self-interactions [55, 56], in addition to its interactions with the Standard Model content. This implies that dark matter is effectively collisionless and dissipationless, lacking any efficient mechanism to cool. As a result, dark matter evolves differently from baryonic matter during cosmic history. Furthermore, without sufficient interactions there is no mechanism yielding

a significant production of dark matter at later times, meaning that dark matter must either be stable or decay on timescales much longer than the age of the universe.

Apart from the measurements of the CMB acoustic peaks discussed above, two other cosmological observations are particularly important in the context of dark matter production: Big Bang Nucleosynthesis [57] and isocurvature perturbations [16], as they constrain both when and how dark matter could have been produced.

Big Bang Nucleosynthesis Independently of CMB data, Big Bang Nucleosynthesis (BBN) probes an even earlier stage of the universe. BBN describes the synthesis of the light elements from free protons and neutrons in the primordial plasma of the early universe. While the predicted abundances depend on several cosmological parameters, the presence of energetic photons capable of breaking apart nuclei makes BBN also sensitive to the baryon-to-photon ratio η, yielding the corresponding best-fit value [33]

$$\eta = (6.2 \pm 0.4) \cdot 10^{-10}, \tag{3.13}$$

which translates to $\Omega_b h^2 = 0.022 \pm 0.002$, with the dimensionless Hubble parameter $h = 0.667$. This is in excellent agreement with the Planck measurements and strengthens confidence in our understanding of cosmic evolution. Since BBN probes an earlier stage of the universe than the CMB, the corresponding temperatures were significantly higher, around $T \sim$ MeV. Any dark matter production mechanism must therefore operate before this epoch.

Iso-curvature perturbations Isocurvature perturbations describe inhomogeneities that differ between particle species without affecting the total energy density. They can arise from independent quantum fluctuations of different fields. A global fit of CMB data shows that such perturbations are subdominant compared to adiabatic perturbations, which affect all species equally. The fact that dark matter and the Standard Model exhibit very similar fluctuations suggests an early connection between the two.

Production

The evolution of the number density n_{DM} of a particle species is governed by the Boltzmann equation. Neglecting the fermionic or bosonic nature of dark matter and assuming identical dark matter particles, it can be approximated in an expanding universe as

$$\dot{n}_{\mathrm{DM}} + 3Hn_{\mathrm{DM}} = -\langle \sigma v_{\mathrm{Møl}} \rangle (n_{\mathrm{DM}}^2 - n_{\mathrm{DM,eq}}^2). \tag{3.14}$$

Here, the right-hand side of the equation represents the annihilation rate of dark matter, given by the thermally averaged annihilation cross section multiplied by the Møller velocity [58], while $n_{\mathrm{DM,eq}}$ denotes the equilibrium number density, typically approximated by the Maxwell–Boltzmann distribution. If the right-hand side becomes negligible, the number of dark matter particles is conserved and is diluted only by the expansion of the universe, which is accounted for by the term $3Hn_{\mathrm{DM}}$ on the left-hand side.

When calculating the dark matter abundance, it is convenient to introduce the quantity Y_{DM}, defined as

$$Y_{\mathrm{DM}} = \frac{n_{\mathrm{DM}}}{s}, \tag{3.15}$$

where s is the total entropy density. The advantage of using this quantity, instead of the number density n_{DM} alone, is that it remains constant whenever the number of dark matter particles per comoving volume is conserved. In other words, Y_{DM} remains constant once dark matter production has ceased and it has decoupled from the Standard Model, provided that no number-changing processes remain active. The present-day value Y_{DM0} can then be estimated from the observed dark matter mass density as

$$\rho_{\mathrm{DM}} = M_{\mathrm{DM}} n_{\mathrm{DM}} = M_{\mathrm{DM}} s_0 Y_{\mathrm{DM0}}, \tag{3.16}$$

with $\rho_{\mathrm{DM}}/s_0 \simeq 0.44$ eV [16] and dependence on the dark matter mass M_{DM}.

Having introduced the relevant framework, we now present two of the most common mechanisms for dark matter production, which arise as natural consequences of the properties and bounds outlined above.

Freeze-out By far, the most popular mechanism for dark matter production is freeze-out [59]. In its simplest form, it assumes that dark matter is a stable particle, weakly interacting with the Standard Model. Although historically dark matter has been considered predominantly in the form of Weakly Interacting Massive Particles (WIMPs), it should be emphasized that the small interaction with the Standard Model does not necessarily have to proceed through the weak force. Nevertheless, the freeze-out mechanism has multiple appealing features. First, it assumes that dark matter was initially in thermal equilibrium with the Standard Model thermal bath in the early universe, when interaction rates exceeded the Hubble expansion rate. This ensures adiabatic initial conditions consistent with the isocurvature perturbation bounds. Second, its only requirement is a sufficiently weakly interacting dark matter particle, typically corresponding to an annihilation cross section typically of order $\langle \sigma v_{\mathrm{Møl}} \rangle = 10^{-26}\ \mathrm{cm^3 s^{-1}}$ [60]. Finally, its simplicity makes it highly predictive: the dark matter density

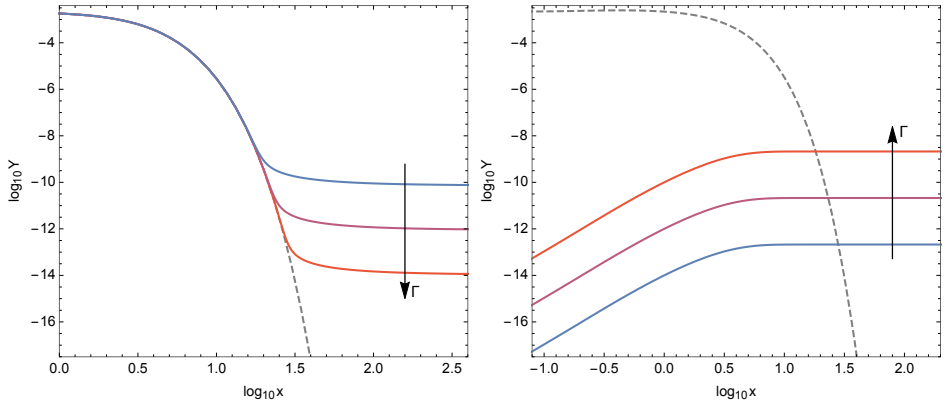

Figure 3.2: Freeze-out (left) and freeze-in (right) evolution of the dark matter abundance for three different values of the annihilation rate Γ, with the arrow indicating the direction of increasing Γ. The variable $x = m_{\mathrm{DM}}/T$ denotes the ratio of the dark matter mass to the temperature. The dashed line represents thermal equilibrium with Standard Model particles, and denotes the ratio of the dark matter mass (or alternatively the mediator mass between the Standard Model and dark matter) to the temperature, which increases as the universe cools. The plots are taken from [61].

can be calculated from just two parameters—the dark matter mass and its interaction cross section with the Standard Model.

As mentioned above, in the freeze-out mechanism, dark matter remains in thermal equilibrium with the ordinary matter thermal bath until its annihilation rate can no longer compete with the Hubble expansion rate, which occurs roughly when

$$\Gamma \sim n_{\mathrm{DM,eq}} \langle \sigma v_{\mathrm{Møl}} \rangle \lesssim H, \tag{3.17}$$

where Γ is the annihilation rate and σ is the total annihilation cross section. Simply put, dark matter becomes too diluted to annihilate efficiently, leaving behind a "frozen" relic abundance that we observe today. Note that stronger interactions reduce the dark matter abundance by increasing the annihilation rate, which keeps dark matter in thermal equilibrium with the thermal bath for a longer time, as illustrated in Figure 3.2. This feature favors couplings that are small enough to remain consistent with current experimental bounds, while still providing a observed dark matter abundance.

Freeze-in A scenario somewhat inverse to freeze-out can occur if the dark matter coupling to the Standard Model content is too small for the dark matter abundance to ever reach thermal equilibrium [62]. In this paradigm, dark matter starts with a negligible density and gradually builds up its

abundance, but the interaction rate drops below the Hubble expansion rate before equilibrium is achieved, and the dark matter abundance "freezes in". In terms of the Boltzmann equation (3.14), this corresponds to the regime $n_{\mathrm{DM,eq}} \gg n_{\mathrm{DM}}$. In this case, the inverse annihilation rate Γ governs the production of dark matter, placing an approximate upper limit on the coupling to the Standard Model at order of 10^{-7}. Above this value, dark matter would thermalize too efficiently. This process is also illustrated in Figure 3.2. The freeze-in scenario remains highly predictive, like freeze-out, but due to its extremely small interactions with the Standard Model it is much harder to test experimentally and therefore often considered less appealing than the latter.

Unlike the freeze-out case, it is not as straightforward to conclude that the inhomogeneities are predominantly adiabatic rather than isocurvature, since freeze-in lacks thermal equilibrium. Nevertheless, in the freeze-in scenario dark matter is produced from the Standard Model thermal bath and therefore inherits its adiabatic perturbations on observable scales. Any possible isocurvature contributions are suppressed and remain well below current observational bounds [63].

(In)direct detection experiments

Over the past several decades, great effort has been devoted to detecting dark matter through its non-gravitational interactions with ordinary matter. Due to the large number of experiments and the variety of approaches, a comprehensive review of all results lies beyond the scope of this thesis. Instead, we highlight some results from the channels most relevant to the present work.

Direct detection aims to observe the energy deposited by dark matter scattering off atoms. The most sensitive experiments include PandaX-4T [65, 66], XENONnT [67, 68] and LUX-ZEPLIN [69]. Because of the extremely low expected event rate, these searches typically employ massive multi-ton, ultra-pure detectors located deep underground, both to increase the probability of scattering events and to reduce background noise. So far, no conclusive evidence has been found, and direct detection experiments have instead provided increasingly stringent bounds on dark matter interactions with nucleons. An overview of these bounds is shown in Figure 3.3, which presents the limits on the spin-independent dark matter–nucleon scattering cross section.

Indirect detection, on the other hand, aims to observe the byproducts of dark matter decay or pair annihilation by measuring cosmic-ray fluxes that exceed the expected contribution from astrophysical sources. Such events are far more common than those in direct detection, but the method suffers

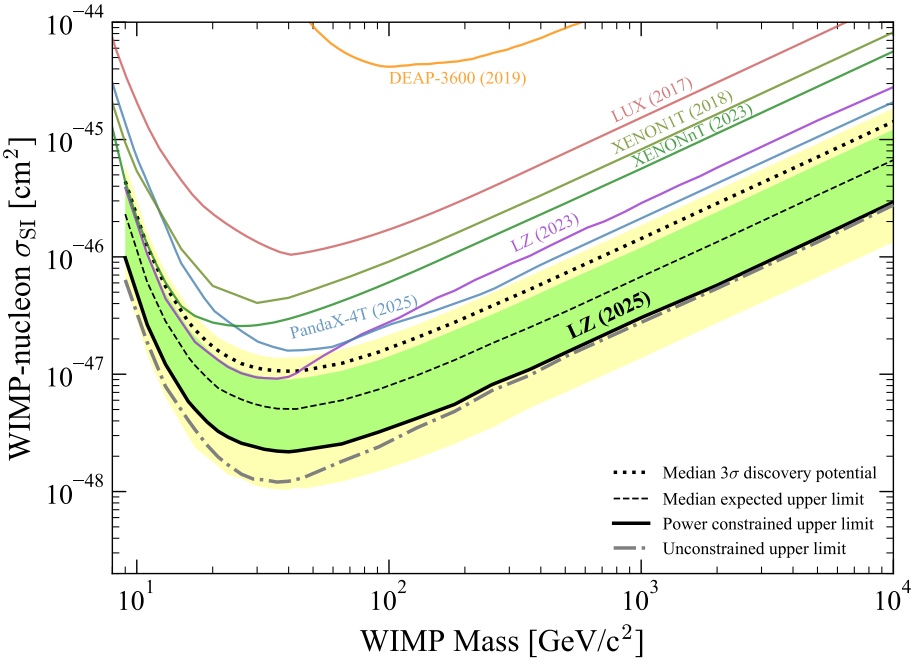

Figure 3.3: Bounds on the dark matter–nucleon scattering cross section. Regions above the solid lines are excluded at the 90% confidence level. The most stringent constraints are provided by LUX-ZEPLIN (LZ), with the 68% and 95% confidence level regions shown in green and yellow, respectively. The plot is taken from [64].

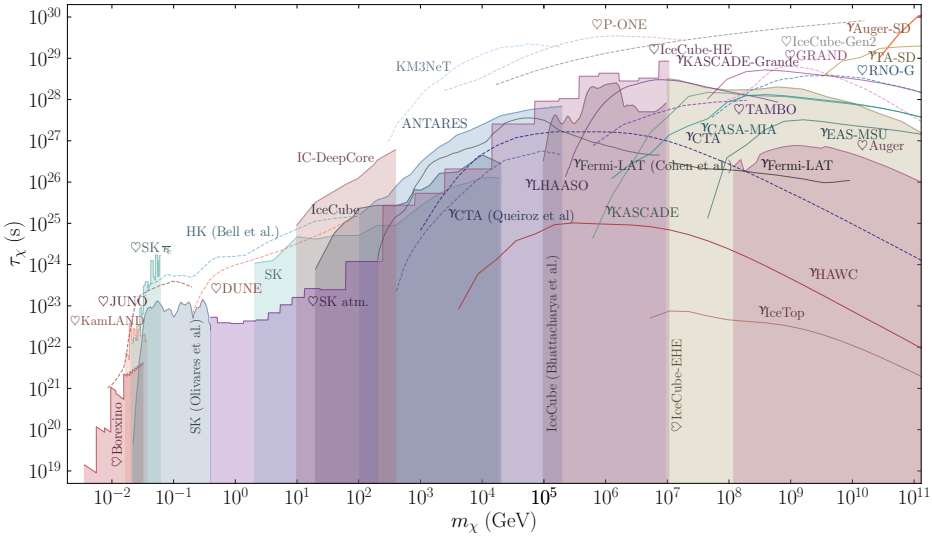

Figure 3.4: Constraints on the lifetime of dark matter with mass m_χ decaying into neutrinos. The shaded region is excluded by neutrino telescope data, while the unshaded region below the solid line is excluded by gamma-ray observatories. Dashed lines indicate the projected sensitivity of future experiments. Plot taken from [73].

from astrophysical uncertainties, since many background processes are not yet well understood. To reduce these uncertainties, indirect detection experiments often focus on rarer channels with lower background noise. The most notable experiments include Fermi-LAT [70], AMS-02 [71] and IceCube [72]. As an important example for this thesis, Figure 3.4 highlights numerous experiments searching for dark matter decay into neutrinos, which place bounds on the dark matter lifetime that are several orders of magnitude longer than the age of the universe across the studied mass range.

3.2 Cosmic inflation

Despite its successes, Big Bang cosmology has serious shortcomings, most notably the horizon problem and the flatness problem [18], which are discussed in more detail in Section 3.2.1. A widely accepted resolution is the so-called inflationary period, proposed prior to the radiation-dominated epoch in the pioneering works of Starobinsky [17], Guth [18], and Linde [19]. The inflationary paradigm postulates a phase of rapid accelerated expansion in the very early universe. This idea not only addresses the aforementioned problems, but also provides solutions to other open questions, such as generating the initial quantum perturbations that seeded the formation of large-scale structure [74, 75].

To produce an accelerated expansion in General Relativity, the energy–momentum tensor must have negative pressure, similar to the case of a cosmological constant. A natural candidate to drive inflation is the false vacuum V of a scalar field ϕ, called the inflaton. With positive vacuum energy, the field provides negative pressure, and after transitioning to the true vacuum, the standard Big Bang cosmology can resume. This transition generally cannot proceed through a first-order phase transition, as that would produce large inhomogeneities [76]. Instead, the vacuum energy V must evolve dynamically to allow for a smooth, second-order–like transition. In Section 3.2.2 we adopt the common assumption that the field acceleration $\ddot{\phi}$ is small, leading to the slow-roll approximation [19]. Finally, we note that inflation can also be described in the framework of modified gravity, as has been widely studied. Although philosophically different, these approaches are often mathematically similar, since modified gravity theories typically reduce to models involving scalar fields [17, 77].

3.2.1 Motivation

The flatness problem

To illustrate the essence of the flatness problem, let us rewrite the Friedmann equations (3.7) in terms of the previously introduced fraction of the critical density, $\Omega_{\text{tot}} = \sum_j \rho_j/\rho_c$, now also including the curvature contribution:

$$\begin{aligned} \Omega_{\text{tot}} - 1 &= \frac{k}{a^2 H^2}, \\ \frac{\ddot{a}}{a} &= -\frac{1}{2} H^2 \Omega_{\text{tot}} (1 + 3w). \end{aligned} \tag{3.18}$$

From these equations, one can derive the evolution of the density parameter Ω_{tot} with the expansion of the universe:

$$\frac{d\Omega_{\text{tot}}}{d \ln a} = (1 + 3w)\Omega_{\text{tot}}(\Omega_{\text{tot}} - 1). \tag{3.19}$$

As seen here, a flat universe ($\Omega_{\text{tot}} = 1$) remains flat. However, for $w > -\frac{1}{3}$ (as in the radiation- or matter-dominated universe), this fixed point is unstable: even small deviations from flatness grow with time. As mentioned above, our universe is consistent with flatness, with deviations from $\Omega_{\text{tot}} = 1$ quantified by the present-day curvature parameter $\Omega_{k,0} = 0.0004(18)$ [41]. Without a physical explanation, the (near-)perfect flatness of the universe appears fine-tuned and, therefore, problematic.

The inflationary period, dominated by a positive potential V corresponding to negative pressure, effectively mimics a cosmological constant

Λ with an equation-of-state parameter $w \simeq -1$ (see section 3.2.2). From Eq. (3.19), one sees that in this regime Ω_{tot} is driven toward the flatness fixed point. If the inflationary expansion lasts long enough, it naturally brings the total energy density close to the critical value, making any subsequent deviation during the radiation- and matter-dominated eras negligible.

The horizon problem

As light travels along a null geodesic, $dr = dt/a$, the comoving distance it covers between times t_1 and t_2 in an expanding universe is

$$\Delta r = \int_{t_1}^{t_2} \frac{dt}{a} = \int_{\ln a_1}^{\ln a_2} \frac{d \ln a}{aH} \tag{3.20}$$

In a radiation- or matter-dominated universe, the expansion is decelerating, and the integrand, the so-called comoving Hubble radius, $(aH)^{-1} = 1/\dot{a}$ converges. As a result, the comoving distance traversed by light since the Big Bang is finite. This defines the particle horizon: regions separated by more than this distance are causally disconnected, as no signal could have traveled between them.

One can estimate the particle horizon from the Big Bang ($a \to 0$) to the time of last scattering of photons observed in the CMB ($a \sim 1/1100$), obtaining a comoving distance of approximately $\Delta r \sim 100$ Mpc, which corresponds to about one degree on the CMB sky today [46]. This implies that photons we observe entering the horizon today originated from regions that were causally disconnected in the early universe. Nevertheless, CMB measurements reveal an almost perfect blackbody radiation spectrum with temperature fluctuations on the level of $\Delta T/T = 10^{-5}$ [16]. If this homogeneity were not an initial condition, it would require an implausible degree of fine-tuning to explain how causally disconnected regions evolved to such similar states. This puzzling uniformity is referred to in the literature as the horizon problem.

Note that the horizon problem arises from the decelerating nature of the radiation- and matter-dominated universe. This means that the comoving Hubble radius $(aH)^{-1}$, which determines the region that is causally connected at a given time, was much smaller in the past. This can be verified by differentiating the scale factor evolution in Eq. (3.10) and substituting the equation-of-state parameter for matter or radiation. The simple solution to make all regions of the CMB causally connected is to introduce a period of accelerated expansion. During such an inflationary epoch, the comoving Hubble radius decreases while the particle horizon continues to grow as the universe expands. By the end of inflation, the comoving Hubble radius lies well within the particle horizon, meaning that all regions corresponding to

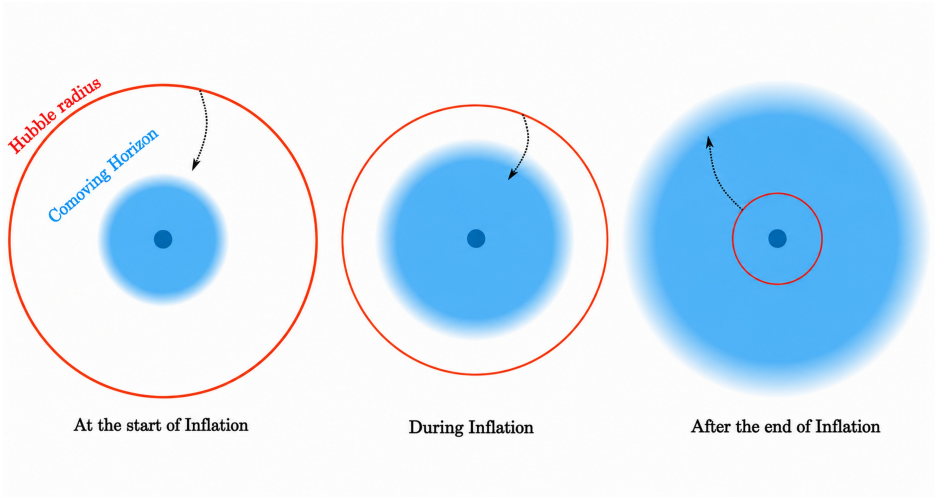

Figure 3.5: Illustration of the effect of the inflationary period on the relationship between the Hubble radius (red) and the particle (comoving) horizon (blue). The black arrow indicates the shrinking of the Hubble radius during inflation and its subsequent expansion in the post-inflationary era. In simple terms, regions within the blue area are causally connected, while the red circle represents the size of the observable universe at a given time. The plot is taken from [47].

the observable universe today were causally connected before the onset of the radiation-dominated era. The relationship between the comoving Hubble radius and the particle horizon is illustrated schematically in Figure 3.5.

To give a rough estimate of the inflationary expansion required to alleviate the horizon problem, one can again examine the comoving Hubble radius by demanding that it were larger at the start of inflation than the observable universe today:

$$(a_{\text{start}} H_{\text{start}})^{-1} > (a_0 H_0)^{-1}. \tag{3.21}$$

This can be rewritten as

$$1 > \frac{a_{\text{start}} H_{\text{start}}}{a_0 H_0} = \frac{a_{\text{start}}}{a_{\text{end}}} \frac{a_{\text{end}}}{a_0} \frac{H_{\text{start}}}{H_0}. \tag{3.22}$$

As we will see in Section 3.2.2, the Hubble parameter decreases slowly during inflation, allowing the approximation $H_{\text{start}} \simeq H_{\text{end}}$, which leads to a slight overestimation of the total expansion required. It is convenient to express the required expansion in terms of the number of e-folds, defined as $N = \ln \frac{a_{\text{end}}}{a_{\text{start}}}$. Taking the logarithm of Eq. (3.22) gives

$$N > \ln \frac{a_{\text{end}}}{a_0} + \ln \frac{H_{\text{end}}}{H_0}. \tag{3.23}$$

Both terms describe the evolution of the universe during the standard Big Bang cosmology and can, in principle, be computed from the conservation of comoving entropy density. Unfortunately, this requires knowledge of the temperature of the universe at the beginning of the radiation-dominated epoch, the so-called reheating temperature T_{RH}. To obtain a very rough estimate, let us assume that the Hubble parameter scales as $H \propto a^{-2}$, as in the radiation-dominated era, and use the fact that the temperature redshifts with the scale factor, $T \propto a^{-1}$. Under these assumptions, Eq. (3.23) simplifies to

$$N \gtrsim \ln \frac{T_{RH}}{T_0}, \tag{3.24}$$

where the present CMB temperature is $T_0 = 10^{-3}$ eV [16]. More rigorous studies of the thermal history of the universe find that the number of e-folds lies in the range $N \simeq 50$–60 [78, 79], corresponding to reheating temperatures between the TeV scale and the grand unification (GUT) scale, $T_{\mathrm{GUT}} = 10^{16}$ GeV.

3.2.2 Slow-roll inflation

By far the most widely used framework for scalar-field–driven inflation is the slow-roll approximation [80], which we outline below. Let us consider a simple action for a scalar field ϕ minimally coupled to gravity:

$$S = \int d^4x\sqrt{-g}\left(\frac{1}{2}M_P^2 R - \frac{1}{2}g^{\mu\nu}\partial_\mu\phi\partial_\nu\phi - V(\phi)\right) \tag{3.25}$$

Although models with a minimal coupling to gravity are often disfavored by observations [16], one can perform a conformal transformation on theories with a non-minimal coupling to bring them to the standard Einstein–Hilbert form [45]. Therefore, the analysis presented in this section applies more generally.

The field can be decomposed into a classical homogeneous background and fluctuations:

$$\phi(t, \vec{x}) = \phi(t) + \delta\phi(t, \vec{x}). \tag{3.26}$$

The near homogeneity of the CMB suggests that these fluctuations are small compared to the background value and can be safely neglected when studying the background evolution of inflation. The corresponding energy–momentum tensor is

$$T_{\mu\nu} = \partial_\mu\phi\partial_\nu\phi - g_{\mu\nu}\left(\frac{1}{2}\partial^\rho\phi\partial_\rho\phi + V(\phi)\right), \tag{3.27}$$

from which one can identify the energy density and pressure of a perfect fluid (see Eq. (3.5)):

$$\begin{aligned} \rho &= \frac{1}{2}\dot{\phi}^2 + V(\phi), \\ \rho &= \frac{1}{2}\dot{\phi}^2 - V(\phi). \end{aligned} \tag{3.28}$$

For the equation-of-state parameter $w = p/\rho \simeq -1$ to hold, the potential energy must dominate over the kinetic term, $V(\phi) \gg \dot{\phi}^2$. Strictly speaking, this condition is not necessary for inflation, as accelerated expansion already occurs for $w < -1/3$. Nevertheless, the stronger condition is more natural: it ensures a sufficiently rapid expansion while keeping the inflationary period finite yet long enough to solve cosmological problems. It also has the practical benefit of greatly simplifying the analysis.

To further ensure a prolonged inflation, maintain the validity of the first slow-roll condition throughout the entire period, and simplify the equations of motion, the second slow-roll condition requires the field acceleration $\ddot{\phi}$ to be also small:

$$\left|\ddot{\phi}\right| \ll \left|3H\dot{\phi}\right|, \left|V'(\phi)\right|, \tag{3.29}$$

where $V'(\phi) = \frac{dV(\phi)}{d\phi}$. Under this approximation, the equation of motion for ϕ derived from the Friedmann equations in Eq. (3.8) simplifies to

$$\ddot{\phi} + 3H\dot{\phi} + V'(\phi) \simeq 3H\dot{\phi} + V'(\phi) = 0. \tag{3.30}$$

It is convenient to define the slow-roll parameters as

$$\begin{aligned} \epsilon &= \frac{M_P^2}{2}\left(\frac{V'(\phi)}{V}\right)^2, \\ \eta &= M_P^2 \frac{V''(\phi)}{V}. \end{aligned} \tag{3.31}$$

The smallness of the slow-roll parameters, $\epsilon, |\eta| \ll 1$, is equivalent to the assumptions introduced above. These parameters can be related, to a good approximation during slow roll, to the time evolution of the Hubble parameter through the Friedmann Eqs. (3.7):

$$\epsilon \simeq -\frac{\dot{H}}{H^2}, \quad \eta \simeq \frac{\ddot{H}}{2H\dot{H}} - \frac{\dot{H}}{H^2}. \tag{3.32}$$

It is straightforward to see that inflation occurs when $\epsilon < 1$, since the comoving Hubble radius decreases when $d(aH)^{-1}/dt = -\ddot{a}/\dot{a}^2 < 0$, while $\epsilon \simeq -\frac{\dot{H}}{H^2} = 1 - a\ddot{a}/\dot{a}^2$. Inflation ends when $\epsilon \simeq 1$, although the slow-roll

approximation no longer holds at that stage. Nevertheless, it is generally understood that the transition from the slow-roll phase to the post-inflationary reheating stage occurs rapidly and does not significantly affect the overall expansion history. The reheating stage refers to the process in which the potential energy of the inflaton field is converted into thermalized particles, restoring the conditions of the standard Big Bang cosmology as the inflaton settles into the true minimum of its potential. There is an open debate within the scientific community regarding the exact nature of reheating, as even the temperature at which it occurs remains uncertain [81, 82]. For the purposes of this thesis, the details of this process are not crucial and will therefore not be discussed further.

3.2.3 Inflationary observables

The most important observables of inflation arise from the quantum fluctuations $\delta\phi(t, \vec{x})$ introduced in Eq. (3.26), which we have so far neglected in our discussion. These fluctuations break the perfect homogeneity of the early universe and leave measurable imprints on the CMB. In particular, the tilt of the scalar perturbation spectrum, n_s, and the relative amplitude of tensor perturbations, r, can be directly related to the slow-roll parameters introduced above. The full derivation of these relations is lengthy and beyond the scope of this thesis; for a more detailed treatment, see for example [46]. In essence, one studies the spectrum $\mathcal{P}_s(k)$ of a gauge-invariant combination of the scalar-field perturbations $\delta\phi(t, \vec{x})$ and the scalar metric perturbations. Similarly, tensor perturbations of the metric give rise to a separate spectrum $\mathcal{P}_t(k)$, which at first order is decoupled from the scalar sector and manifests observationally as a stochastic background of primordial gravitational waves. The ratio of the two spectra defines the tensor-to-scalar ratio r, which under the slow-roll approximation is given by

$$r = \frac{P_t}{\mathcal{P}_s} \simeq 16\epsilon_*, \tag{3.33}$$

where ϵ_* is the slow-roll parameter (defined in Eq. (3.31)) evaluated at the time when the relevant cosmological scales were generated, typically near the beginning of inflation. Moreover, the slow evolution of the Hubble parameter H during inflation induces a weak scale dependence in the spectra, known as the tilt. The tensor tilt is predicted to be very small and remains challenging to detect, whereas the scalar tilt provides a significant observational constraint and is related to the slow-roll parameters as

$$n_s - 1 = \frac{d \ln \mathcal{P}_s}{d \ln k} \simeq -6\epsilon + 2\eta, \tag{3.34}$$

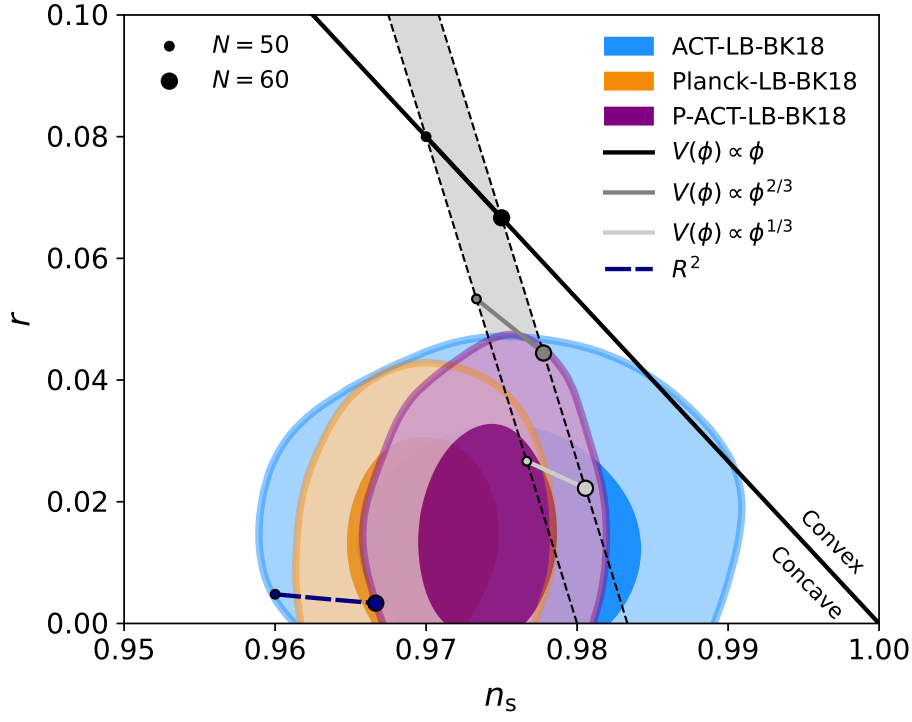

Figure 3.6: Measurements of the scalar spectral index n_s and tensor-to-scalar ratio r at $k = 0.05$ Mpc^{-1} from ACT (blue), Planck 2018 (orange), and their combination (purple). All contours also include data from BICEP2/Keck Array, CMB lensing, and BAO experiments. The inner and outer contours correspond to 68% and 95% confidence levels, respectively. Several benchmark inflationary models are indicated. The plot is taken from [83].

again evaluated at the same stage of inflation. Experiments aiming to measure the inflationary observables n_s and r are very active, with several ongoing and planned missions designed to improve the measurement precision, such as the BICEP and Keck Collaborations [84], LiteBIRD [85], and CMB-S4 [86], among others. The recently completed ACT experiment [83] has also presented new results, shown in Figure 3.6 in combination with other experiments.

Chapter 4

Neutrino masses

As described in Table 2.1, neutrinos belong to the left-handed lepton doublet L_L that transforms under the $SU(2)_L$ symmetry group. Under the remaining gauge group $SU(3)_C \times U(1)_{\mathrm{EM}}$, neutrinos transform as singlets, meaning they do not participate in strong or electromagnetic interactions. Within the Standard Model, whose Lagrangian was introduced in Eq. (2.5), fermions acquire masses after symmetry breaking through Yukawa interactions, as discussed in Section 2.1. The inclusion of right-handed neutrinos formally allows the introduction of a Dirac mass term via fine-tuning of the corresponding Yukawa couplings. Yet, this would only amplify the already large hierarchy in the Higgs couplings, making the approach unsatisfactory.

Experiments on neutrino oscillations, such as Super-Kamiokande [6] (see Section 4.1), have proven that neutrinos possess mass. One could attempt to generate neutrino masses within the Standard Model through loop corrections. The only possibility is to use the $\bar{L}_L L_L^C$ terms, where the charge-conjugated field is defined as $L_L^C = C\bar{L}_L$ with the charge-conjugation matrix C. The problem with such a term is that it violates lepton number, thereby breaking the accidental symmetry of the Standard Model, $U(1)_{\mathrm{B-L}}$. Since this symmetry is anomaly-free, no such term can arise within the Standard Model. Consequently, neutrino oscillation experiments provide conclusive evidence for physics beyond the Standard Model, necessitating its extension to explain neutrino masses.

Treating the Standard Model as an effective low-energy theory valid well below some new physics scale Λ allows one to construct non-renormalizable operators that generate neutrino masses. The lowest-dimension operator of this kind is the dimension-5 Weinberg operator [87]:

$$-\mathcal{L}_{m_\nu} = \left(\bar{L}_L \tilde{H}\right) \frac{\kappa^\nu}{\Lambda} \left(H^T L_L^C\right) + \mathrm{h.c}, \tag{4.1}$$

where κ^ν is a dimensionless coupling constant. This term is permitted because the new physics responsible for it does not have to respect the acciden-

tal symmetries of the Standard Model. Moreover, the smallness of neutrino masses arises naturally from the suppression by the large new-physics scale Λ. The possible ultraviolet completions that generate this operator are discussed in Section 4.2.

4.1 Evidence for neutrino masses

To better understand the evidence for neutrino masses, let us examine the relationship between the neutrino flavor and mass eigenstates, ν_α and ν_i. Following the standard derivation presented in [88], and omitting details not essential for this discussion, we summarize the key steps below.

The time evolution of a massive neutrino state is described by a plane wave:

$$|\nu_i(t)\rangle = e^{-iE_i t}|\nu_i(0)\rangle. \tag{4.2}$$

The flavor and mass eigenstates are connected through a unitary transformation defined by the mixing matrix U (commonly referred to as the Pontecorvo–Maki–Nakagawa–Sakata matrix [89]):

$$|\nu_i\rangle = \sum_{\alpha}^{e,\mu,\tau} U_{\alpha i}|\nu_\alpha\rangle. \tag{4.3}$$

By combining Eqs. (4.2) and (4.3), the time evolution of a neutrino produced in a definite flavor state can be expressed as

$$|\nu_\alpha(t)\rangle = \sum_{i}^{n} U^*_{\alpha i}|\nu_i(t)\rangle = \sum_{i}^{n}\sum_{\beta}^{e,\mu,\tau} U^*_{\alpha i}U_{\beta i}e^{-iE_i t}|\nu_\beta\rangle. \tag{4.4}$$

Eq. (4.4) shows that as the mass eigenstates evolve in time, the flavor states of neutrinos also change. A pure flavor eigenstate at time $t = 0$ thus becomes a superposition of different flavor states at a later time t. Using Eq. (4.4), one can readily compute the probability for a transition $\nu_\alpha \to \nu_\beta$:

$$P_{\alpha\beta} = |\langle\nu_\beta|\nu_\alpha(t)\rangle|^2 = \sum_{i,j}^{n} U^*_{\alpha i}U_{\beta i}U_{\alpha j}U^*_{\beta j}e^{-i(E_i-E_j)t}. \tag{4.5}$$

For all practical purposes, neutrinos are ultrarelativistic, with $|p_i| \simeq |p_j| \simeq E$, allowing the use a good approximation

$$E_i \simeq E + \frac{m_i^2}{2E}, \tag{4.6}$$

and therefore the transition probability can be approximated as

$$P_{\alpha\beta} = |\langle\nu_\beta|\nu_\alpha(t)\rangle|^2 = \sum_{i,j}^{n} U^*_{\alpha i}U_{\beta i}U_{\alpha j}U^*_{\beta j}e^{-i\frac{\Delta m^2_{ij}t}{2E}}, \tag{4.7}$$

with $\Delta m^2_{ij} = m^2_i - m^2_j$. Because neutrinos travel at ultrarelativistic speeds, one can replace the time variable with the propagation distance, $t \to L$, since the travel time cannot be directly measured in experiments. This periodic variation in the probability of neutrino flavor eigenstates is known as neutrino oscillation. The first hints of such oscillations appeared already in 1968 [90, 91], when the observed solar ν_e flux was about one third lower than predicted. The first strong evidence came later from the Super-Kamiokande experiment [6], mentioned above. Note that the oscillation phase, $\Phi = -\frac{\Delta m^2_{ij} L}{2E}$, depends on the mass differences between the neutrino mass eigenstates. If neutrinos were truly massless, no oscillations would occur.

Nowadays, numerous experiments focus on a wide variety of neutrino sources. Because neutrinos have extremely small interaction cross sections, the sources used must be highly intense, and their properties must be well understood to accurately predict the emitted neutrino flux. The main research directions can be summarized according to the origin of the neutrinos:

Solar neutrino experiments Thermonuclear fusion in the Sun produces a high flux of neutrinos with typical energies of the order of 1 MeV. Since reactions such as $4p \to {}^4\mathrm{He} + 2\mathrm{e}^+ + 2\nu_\mathrm{e}$ and other fusion processes involving heavier nuclei generate only electron neutrinos ν_e, the initial flux composition is well understood. Experiments studying solar neutrinos include Borexino [92], which precisely measures the ν_e flux and compares it with predictions from Standard Solar Model calculations; Super-Kamiokande [93], which is primarily sensitive to ν_e neutrinos; and SNO [94, 95], which can distinguish between different neutrino flavors. Neutrino oscillations in matter differ from those in vacuum—a phenomenon exploited, for example, by Super-Kamiokande, which observes a day/night asymmetry since solar neutrinos detected at night must pass through the Earth.

Atmospheric neutrino experiments Cosmic rays interacting with the atmosphere of the Earth produce pions and kaons, which decay and generate neutrinos of all flavors over a wide energy range, from about 100 MeV up to more than 1 TeV. Although the absolute neutrino flux is difficult to calculate precisely, the ratio of fluxes among flavors is better understood, since the decay rates of the parent mesons are well known. Key experiments include Super-Kamiokande and IceCube [7]. In these experiments, determining the direction of the incoming neutrinos is crucial, as the zenith angle corresponds to the travel distance: neutrinos arriving from the opposite side of the Earth traverse about 10^4 km, while those coming from above travel only around 10 km.

Accelerator neutrino experiments Colliding high-energy protons produce mesons, which subsequently decay and generate neutrinos, in a process similar to that occurring in cosmic ray interactions. Accelerator-based neutrino experiments offer a significant advantage: they allow experimentalists to precisely control and determine the location and properties of the neutrino source. Such experiments typically focus on the dominant neutrino flux and position the detector at a distance that maximizes the oscillation probability for a given energy range. The measured flux is then compared with predictions obtained from detailed Monte Carlo simulations. Representative experiments include T2K [96] and NOνA [97].

Reactor antineutrino experiments A byproduct of nuclear fission in reactors is the production of electron antineutrinos, $\bar{\nu}_e$, with energies in the MeV range. The $\bar{\nu}_e$ flux can be predicted either from nuclear data on fission yields and beta-decay chains or by measuring the accompanying electron spectra. As in accelerator-based neutrino experiments, the distance of the detector from the source is crucial. For instance, experiments with baselines of around 1 km can measure the mixing angle between the first and third mass eigenstates, θ_{13} with a precision unattainable by other neutrino sources discussed above. Another ongoing effort of reactor-based experiments is the search for neutrinoless double beta decay, the observation of which would confirm that neutrinos are Majorana fermions—consistent with the mass term introduced in Eq. (4.1). Notable experiments include KamLAND [98], Daya Bay [99], and RENO [8].

The combined results from various neutrino experiments are summarized in Table 4.1. These include the mass-squared differences, Δm^2_{21} and Δm^2_{31}, and the parameters of the mixing matrix U, which describe the mixing angles θ_{ij}between different states and the CP-violating phase δ. Since the absolute values of the neutrino masses are still unknown, the ordering of the mass eigenstates remains undetermined. If the masses follow the same hierarchy as charged leptons and quarks, $m_1 < m_2 < m_3$ the pattern is referred to as normal ordering; conversely, if $m_3 < m_1 < m_2$, it is referred to as inverted ordering. Best-fit values for both scenarios are presented in the table.

Significant effort has also been devoted to determining neutrino masses from cosmological observations, independently of neutrino oscillation experiments—most notably through studies of the CMB, we discussed in Chapter 3. Because neutrinos travel at ultrarelativistic speeds in the early universe, the sum of their masses affects the matter power spectrum by suppressing late-time structure formation. At low redshifts, massive neutrinos become non-relativistic and contribute to the total non-relativistic matter density. So far, all cosmological observations remain consistent with massless

Table 4.1: Best fit of oscillation parameters from global analysis of inflation experiment data with 1σ confidence level with normal and inverse ordering assumption. Data taken from [100].

	Normal ordering	Inverse ordering
$\Delta m^2_{21}[10^{-5}\text{eV}^2]$	$7.50^{+0.22}_{-0.20}$	$7.50^{+0.22}_{-0.20}$
$\lvert\Delta m^2_{31}\rvert[10^{-3}\text{eV}^2]$	$2.55^{+0.02}_{-0.03}$	$2.45^{+0.02}_{-0.03}$
$\theta_{12}[^\circ]$	34.3 ± 1.0	34.3 ± 1.0
$\theta_{13}[^\circ]$	$8.53^{+0.13}_{-0.12}$	$8.58^{+0.12}_{-0.14}$
$\theta_{23}[^\circ]$	49.26 ± 0.79	$49.46^{+0.60}_{-0.97}$
$\delta[^\circ]$	194^{+24}_{-22}	284^{+26}_{-28}

neutrinos, placing an upper limit of $\sum m_\nu < 0.072$ eV [101], which is remarkably close to the lower bound implied by oscillation data, $\sum m_\nu > 0.06$ eV. The same collaboration also reports an effective number of neutrino species of $N_{\text{eff}} = 3.10(17)$, confirming the existence of exactly three generations of light neutrinos.

4.2 Neutrino mass generation

At tree level, there are three possible extensions of the Standard Model that generate the effective operator in Eq. (4.1) [102]. Introducing an $SU(2)_L$ singlet fermion leads to the Type-I seesaw mechanism [103, 104]; adding an $SU(2)_L$ triplet scalar with hypercharge results in the Type-II seesaw mechanism [105, 106]; and introducing an $SU(2)_L$ triplet fermion with exotic hypercharge gives rise to the Type-III seesaw mechanism [107]. Their main features are discussed further in Section 4.2.1. The principal shortcoming of the seesaw framework is its limited testability: although it provides a natural explanation for the smallness of neutrino masses, it typically requires either a very high new-physics scale or extremely small couplings. Several approaches have been proposed to lower the relevant scale and make such scenarios accessible at colliders. In this thesis, we focus on one such possibility — the inverse seesaw mechanism [108], discussed in Section 4.2.2.

4.2.1 Seesaw mechanism

A natural way to extend the Standard Model is to introduce right-handed neutrinos, as realized in the Type-I seesaw mechanism. Since right-handed neutrinos are experimentally known not to interact with the Standard Model gauge fields, they must be fermion singlets, commonly referred to as sterile neutrinos. In principle, there is no restriction on the number of sterile

neutrino states, although at least two are required to account for the observed neutrino oscillations. The most common choice in the literature is to introduce three sterile neutrinos, allowing all three Standard Model neutrinos to acquire mass and maintaining the appealing generational symmetry observed among the other fermions.

The Standard Model Lagrangian can then be extended with neutrino mass terms as

$$-\mathcal{L}m\nu = \bar{N}_R M_D \nu_L + \frac{1}{2}\bar{N}_R M_R N_R^C + \text{h.c.}, \tag{4.8}$$

where the sterile neutrinos are denoted by N_R, with their charge-conjugated fields defined as $N_R^C = C\bar{N}_R^T$. The Dirac mass matrix M_D arises after electroweak symmetry breaking, as in Eq. (2.15), with its elements determined by the neutrino Yukawa couplings:

$$(M_D)_{ij} = Y_{ij}^{\nu}\frac{v_h}{\sqrt{2}}. \tag{4.9}$$

The Majorana mass matrix M_R, on the other hand, corresponds to the Standard Model singlet term and can either be introduced directly as a bare mass term in the Lagrangian or generated dynamically through additional new-physics interactions. Consequently, the Standard Model neutrinos acquire mass at tree level via the diagram shown in Figure 4.1. To determine the values of these masses, it is convenient to rewrite Eq. (4.8) as

$$-\mathcal{L}_{m_\nu} = \frac{1}{2}\begin{pmatrix}\overline{\nu^C}_L & \bar{N}_R\end{pmatrix} M_\nu \begin{pmatrix}\nu_L \\ N_R^C\end{pmatrix} + \text{h.c}, \tag{4.10}$$

with the full neutrino mass matrix given by

$$M_\nu = \begin{pmatrix}0 & M_D^T \\ M_D & M_R\end{pmatrix}. \tag{4.11}$$

This mass matrix can be diagonalized perturbatively in the limit $M_R \gg M_D$ [109]. More concretely, the mixing matrix takes the form

$$W = \begin{pmatrix}\left(I - \frac{1}{2}M_D^*\frac{1}{M_R^*}\frac{1}{M_R}M_D^T\right)U & M_D^*\frac{1}{M_R^*}V \\ -\frac{1}{M_R}M_D^T U & \left(I - \frac{1}{2}\frac{1}{M_R}M_D^T M_D^*\frac{1}{M_R^*}\right)V\end{pmatrix} + \mathcal{O}\left(\epsilon^3\right) \tag{4.12}$$

as derived, for example, in [108]. Here, I denotes the identity matrix, U is the PMNS matrix introduced in Eq. (4.3), and V is the matrix that diagonalizes the sterile neutrino sector. The expansion parameter $\epsilon = M_D/M_R$ is extremely small in generic seesaw mechanism, ensuring that this perturbative approximation remains highly accurate.

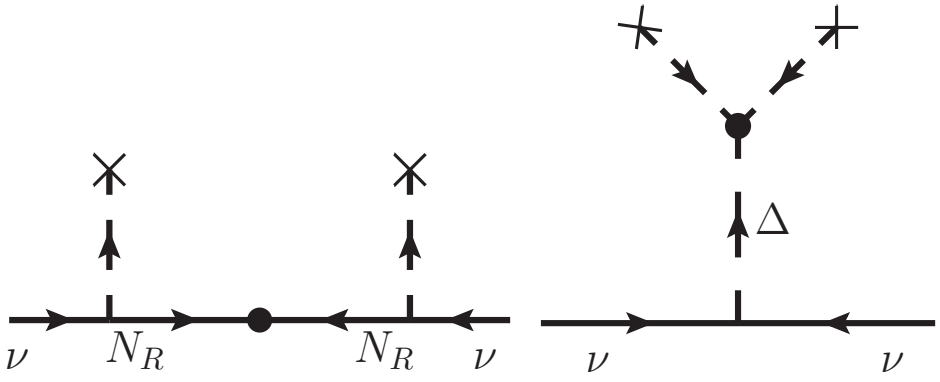

Figure 4.1: Mass generation in the generic Type-I (left) and Type-II (right) seesaw mechanisms. The Type-III diagram is identical to the Type-I case, but with an isotriplet fermion Σ instead of the singlet fermion N_R. The diagrams are taken from [108].

If one uses the mixing matrix from Eq. (4.12) to diagonalize the mass matrix M_ν,

$$W^T M_\nu W = \mathrm{Diag}\left(\nu_1, \nu_2, \nu_3, N_1, N_2, \ldots\right), \tag{4.13}$$

one obtains three light states corresponding to the Standard Model neutrinos and heavy states associated with the sterile neutrinos. Their approximate masses are given by

$$m_\nu \simeq M_D^T \frac{1}{M_R} M_D, \quad M_N \simeq M_R. \tag{4.14}$$

If one assumes the Yukawa couplings Y^ν in Eq. (4.9) to be of order $\mathcal{O}(1)$, then $M_D \sim 100$ GeV. This implies that, to obtain sub-eV masses for the light neutrinos, the Majorana mass term must be at least of the order $M_R \sim 10^{14}$ GeV. While such a scale is appealing from the perspective of leptogenesis and Grand Unified Theories—falling naturally within their energy range—it remains far beyond the reach of current or foreseeable collider experiments.

The Type-III seesaw mechanism is phenomenologically distinct, employing a fermion triplet with nontrivial hypercharge. Nevertheless, the fundamental mass-generation principle remains the same, and a separate discussion is unnecessary for the purposes of this work. The Type-II seesaw mechanism, on the other hand, differs more substantially, as illustrated in Figure 4.1, since it does not require the introduction of new fermions. Instead, the Standard Model neutrinos acquire mass through the vacuum expectation value of a new scalar triplet field Δ,

$$m_\nu = Y^\nu v_\Delta. \tag{4.15}$$

Here, the seesaw suppression arises within the scalar sector itself, as the triplet VEV v_Δ is naturally small—being suppressed by the high mass scale associated with Δ.

4.2.2 Inverse Seesaw mechanism

If we introduce two sets of singlet fermions, N_R and S_L, both carrying lepton number $L = +1$, instead of a single set as in the Type-I seesaw. The part of the Lagrangian that governs neutrino masses then has the form

$$-\mathcal{L}_{m_\nu} = \bar{\nu}_L M_D N_R + \bar{N}_R M_R S_L + \tilde{S}_L \mu S_L + \text{h.c}, \tag{4.16}$$

with $\tilde{S} = S_L^T C^{-1}$ defined using the charge-conjugation matrix C. The Dirac mass term M_D is defined as in Eq. (4.9), as in the usual seesaw case. The term M_R is now also a Dirac mass term, while the Majorana term is μ, which controls lepton-number violation. In the limit $\mu \to 0$, lepton number conservation is recovered. This term can arise from the spontaneous breaking of lepton number (see Section 5.3).

Following the same procedure as in the regular seesaw mechanism and defining the mass matrix M_ν analogously to Eq. (4.11), we obtain, in the (ν_L, N_R^C, S_L) basis,

$$M_\nu = \begin{pmatrix} 0 & M_D^T & 0 \\ M_D & 0 & M_R^T \\ 0 & M_R & \mu \end{pmatrix}. \tag{4.17}$$

Again, by determining the mixing matrix perturbatively in the limit $\mu, M_D \ll M_R$, one obtains

$$W \simeq \begin{pmatrix} U - \frac{1}{2}\frac{1}{M_R} M_D M_D^\dagger \frac{1}{M_R} U & \frac{1}{\sqrt{2}} M_D^\dagger \frac{1}{M_R} & \frac{i}{\sqrt{2}} M_D^\dagger \frac{1}{M_R} \\ 0 & \frac{1}{\sqrt{2}} I & -\frac{i}{\sqrt{2}} I \\ -\frac{1}{M_R} M_D U & \frac{1}{\sqrt{2}}(I - \frac{1}{2}\frac{1}{M_R} M_D M_D^\dagger \frac{1}{M_R}) & \frac{i}{\sqrt{2}}(I - \frac{1}{2}\frac{1}{M_R} M_D M_D^\dagger \frac{1}{M_R}) \end{pmatrix}. \tag{4.18}$$

Using this mixing matrix, we can obtain the mass eigenstates by diagonalizing the mass matrix M_ν (see Eq. (4.13)). This again yields three light neutrinos associated with the Standard Model neutrinos, while the remaining fermions acquire masses at the new-physics scale M_R:

$$m_\nu \simeq M_D \frac{1}{M} \mu \frac{1}{M^T} M_D^T, \quad M_N \simeq M_R. \tag{4.19}$$

Since μ is associated with the lepton-number–violating term, and no other such terms are present, it can naturally take a very small value. Consequently, neutrino masses are suppressed by a small parameter rather than

by a large new-physics scale, which is why this mechanism is referred to as the *inverse* seesaw.

A major advantage of the inverse seesaw mechanism compared to the conventional seesaw is that the new-physics scale does not need to be extremely high. Assuming again that $M_D \sim 100$ GeV, a scale of $M_R \sim 1$ TeV can easily reproduce sub-eV masses for the Standard Model neutrinos if $\mu \sim 10$ eV. Finally, a variety of other schemes are possible, for example, modifying the Type-II or Type-III seesaw mechanisms based on similar principles [108].

Chapter 5

Classically scale-invariant models

As discussed in Section 2.1.1, the Higgs boson mass is sensitive to the scale of new physics and, therefore, appears fine-tuned unless addressed within a beyond-the-Standard-Model framework. One widely studied possibility is to forbid the problematic dimensionful parameters, such as the μ_h^2 term in the Standard Model Lagrangian (Eq. (2.5)), at the tree level [35,110]. In this scenario, symmetry is broken dynamically through a mechanism known as dimensional transmutation, and all masses are generated radiatively through quantum corrections (see Section 5.1). Potentials that contain only dimensionless parameters are referred to as classically scale-invariant potentials, and models based on them are known as classically scale-invariant models.

5.1 Coleman-Gildener-Weinberg formalism

A common approach to studying effective potentials in this framework is the Coleman-Gildener–Weinberg formalism [20, 110]. It is based on the assumption that, along generic field directions, loop corrections are negligible, while along the direction where the tree-level potential vanishes—known as the flat direction—quantum corrections become important, determining the shape and the minimum of the potential. To illustrate the main features of this class of models, let us start with a simple example. Consider a $U(1)$ gauge theory with a complex scalar field $\Phi = (\phi_1 + i\phi_2)/\sqrt{2}$ described by Lagrangian

$$\mathcal{L} = (D_\mu \Phi)^\dagger (D^\mu \Phi) - \frac{1}{4} F^{\mu\nu} F_{\mu\nu} - V(\Phi), \tag{5.1}$$

where the covariant derivative is defined as $D_\mu = \partial_\mu - ieA_\mu$, and $F_{\mu\nu}$ denotes the field strength tensor. The classically scale-invariant potential $V(\Phi)$ is

then given by

$$V(\Phi) = \frac{\lambda}{4!}(\Phi^\dagger \Phi)^2, \tag{5.2}$$

with a dimensionless coupling constant λ. This potential is symmetric and has no minimum away from the origin; thus, it cannot lead to spontaneous symmetry breaking at the classical level. To study the effect of quantum corrections, we now consider the one-loop effective potential. It is useful to define the field norm $\varphi^2 = \Phi^\dagger \Phi = \phi_1^2 + \phi_2^2$, since the effective potential can depend only on gauge-invariant quantities. Even for such a simple model, the full calculation of loop corrections is rather involved and unnecessarily time-consuming. The reader is encouraged to consult the original work by Coleman and Weinberg [110] for a more detailed derivation. Here, we simply present the result in the $\overline{\text{MS}}$ scheme:

$$V_{1-\text{loop}}(\varphi) = \left(\frac{\lambda^2}{256\pi^2} + \frac{3e^4}{64\pi^2}\right)\varphi^4 \left(\ln\frac{\varphi^2}{\mu^2} - \frac{25}{6}\right). \tag{5.3}$$

or the minimum to occur away from the origin, the coupling λ must be small compared to the gauge coupling. In the limit $\lambda^2 \ll e^4$, the effective potential becomes

$$V_{\text{eff}}(\varphi) \simeq \frac{1}{4!}\lambda\varphi^4 + \frac{3e^4}{64\pi^2}\varphi^4 \left(\ln\frac{\varphi^2}{\mu^2} - \frac{25}{6}\right). \tag{5.4}$$

Physical observables cannot depend on the arbitrary renormalization scale μ, so it can be fixed for convenience. The simplest choice is to take $\mu = v_\varphi$, so that the logarithmic term vanishes at the minimum of the potential. The value of the coupling λ at this minimum is obtained from

$$\left.\frac{dV_{\text{eff}}(\varphi)}{d\varphi}\right|_{\varphi=v_\varphi} = 0 \Rightarrow \lambda = \frac{33}{8\pi}e^4. \tag{5.5}$$

Substituting this result into Eq. (5.4), one finds

$$V_{\text{eff}}(\varphi) \simeq \frac{3e^4}{64\pi^2}\varphi^4 \left(\ln\frac{\varphi^2}{v_\varphi^2} - \frac{1}{2}\right). \tag{5.6}$$

Note that we started with the tree-level potential in Eq. (5.2), which contained only the dimensionless coupling λ, and ended up with the effective potential in Eq. (5.6), which introduces the dimensionful parameter v_φ. This replacement of a dimensionless parameter by a dimensionful one is known as dimensional transmutation, as mentioned above. After including radiative corrections, our initially scale-invariant potential becomes associated with a characteristic energy scale v_φ.

To generalize this idea to a general renormalizable gauge theory, let us consider a field vector $\mathbf{\Phi} = (\phi_1, \phi_2, \ldots, \phi_n)^T$ containing n real degrees of freedom. The most general classically scale-invariant potential can then be written as

$$V(\mathbf{\Phi}) = \frac{1}{4!} \sum_{i,j,k,l}^{n} \lambda_{ijkl} \phi_i \phi_j \phi_k \phi_l, \tag{5.7}$$

where λ_{ijkl} is a completely symmetric coupling tensor. As before, we define a radial coordinate φ and also a unit vector $\mathbf{N}$ such that $\mathbf{\Phi} = \varphi \mathbf{N}$. In this case, generally we make no assumptions about the smallness of the couplings. This implies that, in the presence of large classical field contributions, radiative corrections become negligible. However, for dynamical symmetry breaking to occur, there must exist a direction in field space along which the tree-level potential vanishes. As mentioned earlier, this direction corresponds to the flat direction, denoted here by $\mathbf{n}$. The condition for the flat direction to be stationary is

$$\nabla_{\mathbf{N}} V(\mathbf{N})|_{\mathbf{N}=\mathbf{n}} = \sum_{j,k,l} \lambda_{ijkl} n_j n_k n_l = 0. \tag{5.8}$$

For the flat direction to correspond to a local minimum, the Hessian matrix

$$(\mathbf{P})_{ij} = \left. \frac{\partial^2 V(\mathbf{N})}{\partial N_i \partial N_j} \right|_{\mathbf{N}=\mathbf{n}} = \frac{1}{2} \sum_{k,l} \lambda_{ijkl} n_k n_l \tag{5.9}$$

must be positive semidefinite, meaning it satisfies the condition $\mathbf{x}^T \mathbf{P} \mathbf{x} \geq 0$ for all $\mathbf{x} \in \mathbb{R}^{\dim(\mathbf{P})}$. As before, we omit the detailed derivation of the radiative corrections and note that, in the $\overline{\text{MS}}$ scheme, the one-loop correction takes the form

$$V^{(1)}(\varphi \mathbf{n}) = A(\mathbf{n}) \varphi^4 + B(\mathbf{n}) \varphi^4 \ln \frac{\varphi^2}{\mu^2}, \tag{5.10}$$

where the coefficients $A(\mathbf{n})$ and $B(\mathbf{n})$ depend on the radiatively induced minimum v_φ and on the tree-level field masses:

$$\begin{aligned} A(\mathbf{n}) = \frac{1}{64\pi^2 v_\varphi^4} \Bigg\{ & \operatorname{tr} \left[\mathbf{m}_S^4 \left(\ln \frac{\mathbf{m}_S^2}{v_\varphi^2} - \frac{3}{2} \right) \right] \\ & + 3 \operatorname{tr} \left[\mathbf{m}_V^4 \left(\ln \frac{\mathbf{m}_V^2}{v_\varphi^2} - \frac{5}{6} \right) \right] \\ & - 4 \operatorname{tr} \left[\mathbf{m}_F^4 \left(\ln \frac{\mathbf{m}_F^2}{v_\varphi^2} - \frac{3}{2} \right) \right] \Bigg\}, \end{aligned} \tag{5.11}$$

$$B(\mathbf{n}) = \frac{1}{64\pi^2 v_\varphi^4} \left(\operatorname{tr} \mathbf{m}_S^4 + 3 \operatorname{tr} \mathbf{m}_V^4 - 4 \operatorname{tr} \mathbf{m}_F^4 \right), \tag{5.12}$$

where the subscripts S, V, F denote scalar, vector, and fermion fields, respectively. As in the derivation of Eq. (5.6), we can fix the arbitrary renormalization scale and minimize Eq. (5.10) with respect to φ. Choosing $\mu = \exp(\frac{A}{2B} + \frac{1}{4})$ gives

$$V^{(1)}(\varphi\mathbf{n}) = B(\mathbf{n})\varphi^4 \left(\ln \frac{\varphi^2}{v_\varphi^2} - \frac{1}{2} \right). \tag{5.13}$$

With the coefficient $B(\mathbf{n}) > 0$, the radiatively induced minimum lies below the classical one, located at the origin where $V(\mathbf{0}) = 0$. As a final but important remark, let us examine the scalar masses. Using the previously defined Hessian matrix in Eq. (5.9), the tree-level scalar masses can be written as

$$\mathbf{m}_S^2 = v_\varphi^2(\mathbf{P})_{ij}, \tag{5.14}$$

while including the radiative corrections gives

$$(\mathbf{m}_S^2 + \delta\mathbf{m}_S^2)_{ij} = \left. \frac{\partial^2[V(\mathbf{\Phi}) + V^{(1)}(\mathbf{\Phi})]}{\partial\phi_i\partial\phi_j} \right|_{\mathbf{\Phi}=v_\varphi\mathbf{n}}. \tag{5.15}$$

For scalar fields orthogonal to the flat direction, quantum corrections are expected to be small and can safely be neglected. In contrast, the field along the flat direction, called the dilaton, does not acquire a tree-level mass, since by definition the tree-level potential vanishes there. However, it receives a mass radiatively, given by

$$m_\varphi^2 = 8B(\mathbf{n})v_\varphi^2. \tag{5.16}$$

In their original proposal, Coleman and Weinberg [110] suggested that electroweak symmetry could be broken dynamically, identifying the dilaton with the Higgs boson and thereby explaining its lightness. This idea, however, has been ruled out experimentally within the Standard Model [34], necessitating an extension of the scalar sector. Beyond-the-Standard-Model scenarios face similar challenges in realizing the Higgs as a dilaton, as it is difficult to satisfy both experimental and theoretical constraints, particularly without invoking non-perturbative couplings. In Section 5.4, we explore the possibility of a naturally light Higgs boson that is not a dilaton.

5.2 Flat directions in scale-invariant potentials

In our paper [111], we introduced a new technique to investigate the appearance of flat directions, which is considerably simpler than the more commonly used approach based on hyperspherical coordinates. We begin

by reviewing the simpler case of biquadratic potentials and then extend our discussion to the general potential form given in Eq. (5.7). The general biquadratic potential can be written as

$$V(\mathbf{\Phi}) = \sum_{i,j}^{n} \phi_i^2 \lambda_{ij} \phi_j^2 = (\mathbf{\Phi}^{\circ 2})^T \mathbf{\Lambda} \mathbf{\Phi}^{\circ 2}, \tag{5.17}$$

where $\mathbf{\Lambda}$ is a symmetric coupling matrix. The symbol $\circ$ denotes the Hadamard product, defined as the element-wise product of matrices, $(\mathbf{A} \circ \mathbf{B})_{ij} = A_{ij} B_{ij}$. The Hadamard power is then given by $(\mathbf{A}^{\circ n})_{ij} = A_{ij}^n$, implying that $\mathbf{\Phi}^{\circ 2} = (\phi_1^2, \phi_2^2, \ldots, \phi_n^2)^T$.

For the potential to be bounded from below, $V(\mathbf{\Phi}) \geq 0$, he necessary and sufficient condition is that the matrix $\mathbf{\Lambda}$ be copositive [112]. This condition can be verified using the Cottle-Habetler-Lemke theorem [113], which states: Suppose that the order $n-1$ principal submatrices of a real symmetric matrix $\mathbf{A}$ of order n are copositive, i.e. $\mathbf{x}^T \mathbf{\Lambda} \mathbf{x} \geq 0$ for all $\mathbf{x} \geq 0$.[1] Then $\mathbf{A}$ is copositive if and only if

$$\det(\mathbf{A}) \geq 0 \quad \vee \quad \text{some element(s) of } \operatorname{adj} \mathbf{A} < 0. \tag{5.18}$$

The adjugate of the matrix $\mathbf{A}$, denoted adj $\mathbf{A}$, is defined through the relation $\mathbf{A} \operatorname{adj}(\mathbf{A}) = \det(\mathbf{A})\, \mathbf{I}$.

We can express the norm of $\mathbf{\Phi}$ using the Hadamard square and the identity element of the Hadamard product, namely the vector of ones $\mathbf{e} = (1, 1, .., 1)^T$, as

$$\mathbf{\Phi}^T \mathbf{\Phi} = \mathbf{e}^T \mathbf{\Phi}^{\circ 2}. \tag{5.19}$$

We restrict the potential in Eq. (5.17) to the unit hypersphere by introducing a Lagrange multiplier, as

$$V(\mathbf{N}, \lambda) = (\mathbf{N}^{\circ 2})^T \mathbf{\Lambda} \mathbf{N}^{\circ 2} + \lambda (1 - \mathbf{e}^T \mathbf{N}^{\circ 2}). \tag{5.20}$$

While the vector $\mathbf{N}$ lies on the unit hypersphere, its Hadamard square $\mathbf{N}^{\circ 2}$ lies on the unit simplex, with its elements serving as barycentric coordinates, as illustrated in Figure 5.1. Minimizing the potential on the unit hypersphere is therefore equivalent to minimizing a quadratic function of $\mathbf{N}^{\circ 2}$ on the unit simplex, given by

$$\frac{\partial V(\mathbf{N}, \lambda)}{\partial \lambda} = 1 - \mathbf{e}^T \mathbf{N}^{\circ 2} = 0, \tag{5.21}$$

$$\nabla_{\mathbf{N}} V(\mathbf{N}, \lambda) = 2\mathbf{N} \circ (2\mathbf{\Lambda} \mathbf{N}^{\circ 2} - \lambda \mathbf{e}) = 0. \tag{5.22}$$

[1] Note that this differs from the usual positive semidefiniteness defined for all real $\mathbf{x}$.

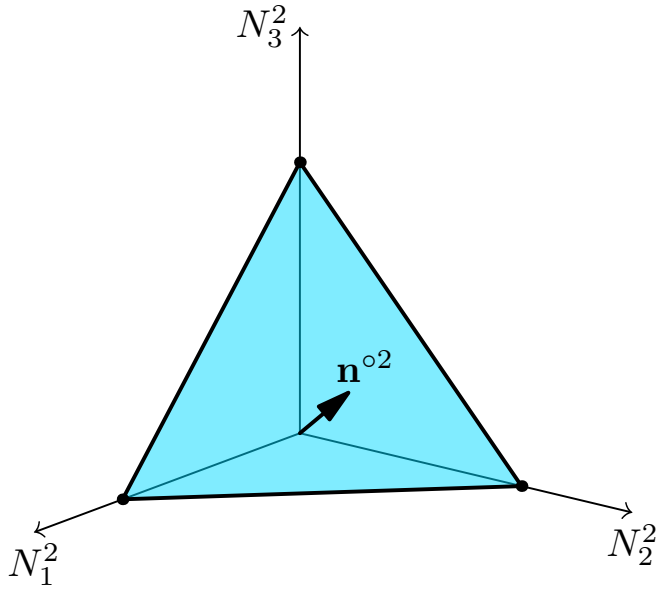

Figure 5.1: The unit simplex for three scalar fields, showing one possible orientation of the flat-direction unit vector's Hadamard square, $\mathbf{n}^{\circ 2}$. Illustration taken from [111].

By assuming that no element of $\mathbf{N}^{\circ 2}$ vanishes, we can combine these two equations as

$$\mathbf{\Lambda}\mathbf{N}^{\circ 2} = \left[(\mathbf{N}^{\circ 2})^T \mathbf{\Lambda}\mathbf{N}^{\circ 2}\right] \mathbf{e} \equiv V(\mathbf{N})\, \mathbf{e}, \tag{5.23}$$

which can then be solved by introducing an ansatz

$$\mathbf{N}^{\circ 2} = \frac{\mathrm{adj}(\mathbf{\Lambda})\, \mathbf{e}}{\mathbf{e}^T \mathrm{adj}(\mathbf{\Lambda})\, \mathbf{e}}, \tag{5.24}$$

where the denominator is simply a normalization factor, given by the sum of all elements of the matrix $\mathrm{adj}(\mathbf{\Lambda})$. From the definition of the adjugate matrix, it is easy to see that the potential value at the extremum then is

$$V(\mathbf{N}) = \frac{\det(\mathbf{\Lambda})}{\mathbf{e}^T \mathrm{adj}(\mathbf{\Lambda}) \mathbf{e}}. \tag{5.25}$$

Finally, the flat direction requires the tree-level potential to vanish along it. From Eq. (5.25), one can see that this condition corresponds to a vanishing determinant of the coupling matrix:

$$\det(\mathbf{\Lambda}) = 0 \overset{0<\mathbf{n}^{\circ 2}<\infty}{\Longleftrightarrow} V(\mathbf{n}) = 0. \tag{5.26}$$

The flat direction is then given by the solution of the minimization equation:

$$\mathbf{n}^{\circ 2} = \frac{\mathrm{adj}(\mathbf{\Lambda})\, \mathbf{e}}{\mathbf{e}^T \mathrm{adj}(\mathbf{\Lambda})\, \mathbf{e}}. \tag{5.27}$$

Eq. (5.26) and Eq. (5.27) are core results of our paper [111], which allow to identify the existence and direction of flat direction with simple conditions. This is illustrated with a concrete model in Section 5.3. There, we also show that it is convenient to define the flat direction as the eigenvector of the coupling matrix $\mathbf{\Lambda}$ associated with a vanishing tree-level mass. The values of the couplings can then be determined from the scalar masses and the flat direction as

$$\mathbf{\Lambda} = \frac{1}{8}\mathbf{P} \circ (\mathbf{n}\mathbf{n}^T)^{\circ -1} = \frac{1}{8v_\varphi^2}\mathbf{m}_S^2 \circ (\mathbf{n}\mathbf{n}^T)^{\circ -1}. \tag{5.28}$$

Finally, for a general potential as in Eq. (5.7), one can follow a similar procedure using the tensor eigenvalue formalism instead of matrix algebra. This yields analogous results, where the existence of a flat direction is ensured by the vanishing of the resultant $\mathrm{res}_{\mathbf{N}}(\mathbf{\Lambda N}^3) = 0$, also known as the hyperdeterminant.

5.3 Radiative inverse seesaw

In this section, we outline the framework of our paper [114], where we investigated the possibility of realizing the inverse seesaw mechanism (described in Section 4.2.2) within a dynamical symmetry breaking model, and proposed a viable dark matter and inflaton candidate within this context. Our primary goal here is to demonstrate the practical application of the method presented in the previous section, while omitting the detailed outcomes of the calculations, which can be found in the paper itself.

As mentioned earlier, the realization of the inverse seesaw mechanism requires introducing two sets of singlet fermions, N_R and S_L. To generate the necessary mass terms after symmetry breaking, the scalar sector is extended by two additional scalar fields. In addition to the Higgs doublet H, the model now includes a complex singlet σ and a real singlet ρ. The relevant part of the Lagrangian responsible for neutrino mass generation is

$$\mathcal{L}_\nu = -Y_D^{ij}\bar{L}_L^j i\tau_2 H^* N_R^i - Y_{NS}^{ij}\rho\bar{N}_{R_i}S_{L_j} - Y_S^{ij}\sigma\tilde{S}_{L_i}S_{L_j} + \text{h.c.} \tag{5.29}$$

One can see that this Lagrangian reproduces the form of Eq. (4.16) after symmetry breaking, with $M_D^{ij} = Y_D^{ij}v_h$, $M^{ij} = Y_{NS}^{ij}v_\rho$ and $\mu^{ij} = Y_S^{ij}v_R$, where $v_h = \langle H\rangle$, $v_\rho = \langle\rho\rangle$, and $v_R = \langle\sigma\rangle$ are the vacuum expectation values of the scalar fields. The scalar field σ carries lepton number $L = -2$, meaning that its Yukawa interaction term breaks lepton number once symmetry is spontaneously broken.

Under the discrete symmetry transformations $\rho \to -\rho$, $\sigma \to -\sigma$ and $\sigma \to \sigma^*$, the scale-invariant potential is

$$\begin{aligned} V = {} & \lambda_H |H|^4 + \lambda_\sigma |\sigma|^4 + \frac{1}{4}\lambda_\rho \rho^4 + \lambda_{H\sigma}|H|^2|\sigma|^2 + \frac{1}{2}\lambda_{H\rho}|H|^2\rho^2 + \frac{1}{2}\lambda_{\rho\sigma}|\sigma|^2\rho^2 \\ & + \frac{1}{2}\lambda'_{H\sigma}(\sigma^2 + \sigma^{*^2})|H|^2 + \frac{1}{4}\lambda'_{\rho\sigma}(\sigma^2 + \sigma^{*^2})\rho^2 + \frac{1}{2}\lambda'_\sigma(\sigma^4 + \sigma^{*^4}) \\ & + \frac{1}{2}\lambda''_\sigma(\sigma^2 + \sigma^{*^2})|\sigma|^2. \end{aligned} \tag{5.30}$$

Here, the couplings with primes explicitly break lepton number and generate a mass for the pseudo-Goldstone boson, referred to as the Majoron, which we denote by J in the following. The field J serves as a viable dark matter candidate since it does not mix with other scalar fields, being the only CP-odd state. Nevertheless, J is not entirely stable, as it can decay through the Yukawa sector into neutrinos. As discussed in Section 3.1.1, this does not exclude the possibility of J constituting dark matter, provided that its decay is sufficiently slow. This condition can be achieved for a small dark matter mass (we considered the sub-GeV case) and large values of v_R ($v_R \gtrsim 10^{13}$ GeV in the considered scenario).

It is convenient to parametrize potential in Eq (5.30) as

$$\begin{aligned} V = {} & \frac{1}{4}\lambda_H h^4 + \frac{1}{4}\lambda_\rho \rho^4 + \frac{1}{4}\lambda_R R^4 + \frac{1}{4}\lambda_J J^4 + \frac{1}{4}\lambda_{RJ} R^2 J^2 + \frac{1}{4}\lambda_{H\rho} h^2 \rho^2 \\ & + \frac{1}{4}\lambda_{HR} h^2 R^2 + \frac{1}{4}\lambda_{HJ} h^2 J^2 + \frac{1}{4}\lambda_{\rho R} R^2 \rho^2 + \frac{1}{4}\lambda_{\rho J} J^2 \rho^2, \end{aligned} \tag{5.31}$$

where the original scalar fields have been defined as

$$|H|^2 = \frac{h^2}{2}, \qquad \sigma = \frac{R + iJ}{\sqrt{2}}. \tag{5.32}$$

We can relate the scalar fields that mix with each other in the gauge basis to the mass eigenstates through a rotation matrix

$$\mathbf{O} = \begin{pmatrix} c_{12}c_{13} & s_{12}c_{13} & s_{13} \\ -s_{12}c_{23} - c_{12}s_{23}s_{13} & c_{12}c_{23} - s_{12}s_{23}s_{13} & s_{23}c_{13} \\ s_{12}s_{23} - c_{12}c_{23}s_{13} & -c_{12}s_{23} - s_{12}c_{23}s_{13} & c_{23}c_{13} \end{pmatrix}, \tag{5.33}$$

where the rotation angles α_{ij} are absorbed into the shorthand notation $s_{ij} \equiv \sin\alpha_{ij}$ and $c_{ij} \equiv \cos\alpha_{ij}$. Then gauge and mass eigenstates are related as

$$\begin{pmatrix} h \\ \rho \\ R \end{pmatrix} = \mathbf{O} \begin{pmatrix} h_1 \\ h_2 \\ h_3 \end{pmatrix}, \tag{5.34}$$

One of the mass eigenstates must correspond to the Standard Model Higgs boson with $m_h = 125.1$ GeV. In our paper, we identified this state with h_1, while h_3 was associated with the dilaton, which has a vanishing tree-level mass. Consequently, the flat direction must align with the eigenvector corresponding to h_3, i.e., the last column of the matrix $\mathbf{O}$:

$$\mathbf{n} = \begin{pmatrix} s_{13} \\ s_{23}c_{13} \\ c_{23}c_{13} \end{pmatrix}. \tag{5.35}$$

Now that the flat direction has been identified, the couplings of the CP-even scalar fields can be expressed in terms of physical parameters using Eq. (5.28). The corresponding coupling matrix in that equation is

$$\mathbf{\Lambda} = \frac{1}{4}\begin{pmatrix} \lambda_H & \frac{1}{2}\lambda_{H\rho} & \frac{1}{2}\lambda_{HR} \\ \frac{1}{2}\lambda_{H\rho} & \lambda_\rho & \frac{1}{2}\lambda_{\rho R} \\ \frac{1}{2}\lambda_{HR} & \frac{1}{2}\lambda_{\rho R} & \lambda_R \end{pmatrix}, \tag{5.36}$$

written in the $(h, \rho, R)^T$ basis. Note that identifying one mass eigenstate with a vanishing mass automatically satisfies the necessary condition for the existence of a flat direction outlined in Eq. (5.26).

The remaining couplings associated with the Majoron J do not affect the flat direction and can be chosen to yield the desired mass,

$$m_J^2 = \tfrac{1}{2}\left(\lambda_{HJ}v_h^2 + \lambda_{\rho J}v_\rho^2 + \lambda_{RJ}v_R^2\right), \tag{5.37}$$

while simultaneously ensuring that lepton number violation remains small.

For a detailed analysis of the constraints and the viable parameter space, the reader is referred to the original paper [114].

5.4 Multi-phase dynamical symmetry breaking

Since no additional scalar fields have been observed experimentally, the dilaton must generally be much heavier than the Higgs boson in classically scale-invariant models. This reduces the model's appeal, as the naturalness of the Higgs mass once again becomes questionable. Although the issue is less severe than in the Standard Model (as discussed in Section 2.1.1), it still appears unnatural that the dilaton—whose mass arises solely from quantum corrections—is significantly heavier than the Higgs boson, whose mass originates at tree level.

One possible way to obtain a naturally light Higgs boson mass is through the framework of dynamical symmetry breaking near a multi-phase critical point. In this scenario, the Higgs mass becomes loop-suppressed in a manner

similar to the dilaton mass. We outline the main features of this framework, first introduced in [115], by examining the model with the dark matter candidate developed in our work [116].

Consider a scale-invariant extension of the Standard Model with two real singlet scalar fields,s and s', endowed with a discrete symmetry $\mathbb{Z}_2 \otimes \mathbb{Z}_2'$. Its potential is

$$V = \lambda_H |H|^4 + \frac{\lambda_S}{4} s^4 + \frac{\lambda_{S'}}{4} s'^4 + \frac{\lambda_{HS}}{2} |H|^2 s^2 + \frac{\lambda_{HS'}}{2} |H|^2 s'^2 + \frac{\lambda_{SS'}}{4} s^2 s'^2. \tag{5.38}$$

We associate s' with dark matter and therefore require that the corresponding $\mathbb{Z}_2'$ symmetry remain unbroken to ensure stability. The other new scalar field, s, breaks its $\mathbb{Z}_2$ symmetry and acquires a vacuum expectation value v_s. In this regime, there are three possible phases of symmetry breaking:

h) $v_h \neq 0$ and $v_s = 0$ occurs when running of the couplings crosses $\lambda_H = 0$ while λ_S,$\lambda_{HS} > 0$ for vacuum stability. From the symmetry-breaking perspective, this reduces the model to the original Coleman–Weinberg proposal [110], which, as already noted, is experimentally excluded.

s) Similarly, $v_s \neq 0$ and $v_h = 0$ occurs when running of the couplings crosses $\lambda_S = 0$ while $\lambda_H, \lambda_{HS} > 0$. This phase is incompatible with the present day because the Higgs boson is known to have a nonzero vacuum expectation value.

sh) Both scalar fields acquire vacuum expectation values, $v_s, v_h \neq 0$. This happens when $\lambda_{HS} = -2\sqrt{\lambda_H \lambda_S} < 0$ with $\lambda_H, \lambda_S > 0$. Contrary to the other two phases, the mass eigenstates are now mixtures of the two gauge eigenstates. This phase is compatible with current constraints.

In the usual Gildener–Weinberg approximation described in Section 5.1, the flat direction in the *sh*) phase is

$$h/s = \sqrt{-\lambda_{HS}/2\lambda_H}, \tag{5.39}$$

where only quantum corrections along this direction are taken into account. We now focus on the interesting case in which symmetry breaking occurs near the intersection of the *sh*) and *s*) phases. This boundary corresponds to the condition

$$\lambda_S(\bar{\mu}) = \lambda_{HS}(\bar{\mu}) = 0. \tag{5.40}$$

Note that on this boundary the Higgs boson is massless, while near the boundary, where the latter condition holds only approximately, it acquires a small mass and is therefore phenomenologically well motivated. In this

multi-phase criticality scenario, due to the smallness of λ_{HS}, one must also include quantum corrections to it, which are ignored in the Gildener–Weinberg approximation. Intuitively: whereas the Gildener–Weinberg approach assumes a flat direction along a straight line, near the phase boundary this approximation breaks down and the flat direction follows a curved trajectory instead. As a consequence, the minimum is displaced in field space.

Interestingly, in the present model, the running of the couplings λ_S and λ_{HS} is mainly driven by their couplings to the dark matter field s'. The dominant contributions to their β-functions are

$$\beta_{\lambda_{HS}} \simeq \frac{1}{2}\lambda_{SS'}\lambda_{HS'}, \qquad \beta_{\lambda_S} \simeq \frac{1}{4}\lambda_{SS'}^2. \tag{5.41}$$

As a result, the dark matter field directly influences the dynamics of symmetry breaking, unlike in the conventional Gildener–Weinberg approximation. Importantly, the coupling $\lambda_{HS'}$, which would otherwise play a role only in dark matter phenomenology—particularly in direct detection—now also becomes crucial as it drives the radiative corrections. The scalar field masses can then be well approximated by

$$m_h^2 \simeq -\frac{\beta_{\lambda_{HS}}}{(4\pi)^2} v_s^2 \ln R, \tag{5.42}$$

$$m_s^2 \simeq 2\frac{\beta_{\lambda_S}}{(4\pi)^2} v_s^2, \tag{5.43}$$

$$m_{s'}^2 \simeq \frac{1}{2}\lambda_{SS'} v_s^2, \tag{5.44}$$

where the parameter $\ln R$ is related to displacement of minimum as

$$\frac{h_{\text{flat}}}{s_{\text{flat}}} \Bigg/ \frac{v_h}{v_s} = \sqrt{1 + \frac{1}{2\ln R}}. \tag{5.45}$$

This approach not only provides a natural explanation for the lightness of the Higgs boson—whose mass arises from quantum corrections, similar to the dilaton—but also yields a viable dark matter candidate and establishes a strong connection between dark matter and Higgs phenomenology. A detailed discussion of the phenomenological implications and experimental constraints can be found in the original paper [116].

Chapter 6

Conclusion

In this thesis, we reviewed the open problems of the standard models of particle physics and cosmology, such as the nature of dark matter, inflation, vacuum stability, neutrino mass generation, and the possible unnaturalness of the Higgs boson mass. To alleviate the latter issue, we explored classically scale-invariant models as a solution. Although this class of models has been known for over 50 years, we demonstrated that there is still room for improvement within this framework.

In our first publication [111], we developed a new method for determining flat directions in scale-invariant potentials. We demonstrated that, for biquadratic potentials, the determinant of the quartic coupling matrix vanishes in the presence of a flat direction. Building on this result, we derived a convenient way to obtain the Hessian matrix when the couplings and the desired flat direction are known, or conversely, to determine the necessary couplings from the scalar masses and the chosen flat direction. We further generalized our findings to generic quartic potentials using the formalism of tensor eigenvalues and provided explicit examples: two- and three-field cases for quartic potentials, and a two-field case for the general one. This new approach greatly simplifies the study of complex scalar sectors, enabling a more straightforward phenomenological analysis of intricate models.

In our second publication [116], we studied a classically scale-invariant model featuring an extended scalar sector with two real gauge singlets. In this model, we explored the regime of multi-phase criticality, where the quantum corrections neglected in the usual Gildener–Weinberg approach become relevant. In this limit, we found a strong connection between dark matter and Higgs phenomenology, as the couplings to dark matter drive the dynamics of symmetry breaking. Consequently, the Higgs boson mass becomes loop-suppressed in a manner similar to the dilaton mass. We showed that the model can be described with only three free parameters and determined the parameter space consistent with experimental constraints such as

direct detection limits and the Higgs boson invisible width, while simultaneously producing the correct dark matter relic abundance and maintaining perturbativity. We also studied the renormalization group running of the couplings to identify the energy scale up to which the theory remains perturbative.

In our third publication [114], we analyzed an inverse seesaw model with a classically scale-invariant potential, featuring one complex and one real scalar singlet in addition to the Standard Model Higgs doublet. In this framework, the imaginary part of the complex singlet—the Majoron—acquires its mass through explicit breaking of lepton number in the potential. We applied the results of our first publication to determine the conditions for the flat direction. To explore the parameter space of the model, we performed a Markov Chain Monte Carlo scan, taking into account experimental constraints such as the Higgs boson signal strength and invisible decay width, the correct neutrino masses, as well as theoretical constraints including perturbativity and vacuum stability. We investigated the possibility of the Majoron serving as a dark matter candidate by scanning the region where, in addition to the previous requirements, the model yields the correct relic abundance while ensuring dark matter stability on cosmological time scales. The latter required a large dilaton vacuum expectation value, which in turn suppressed dark matter interactions, rendering the freeze-out mechanism ineffective. However, we found that the freeze-in mechanism can successfully produce the observed relic abundance. Analyzing typical interaction strengths in this regime, we identified the Standard Model Higgs boson and the new real scalar singlet as viable inflaton candidates. Since Higgs inflation has already been extensively studied, we focused our analysis on the new scalar field. We demonstrated that this model can simultaneously account for neutrino masses, dark matter, and inflation while remaining consistent with both experimental and theoretical constraints.

All three publications aimed to advance the understanding of classically scale-invariant models and to explore their potential for addressing open questions of the Standard Model and cosmology, with particular emphasis on dark matter phenomenology.

Peatükk 7

Kokkuvõte: Dünaamiline sümmeetria rikkumine ja tumeaine

Käesolevas väitekirjas käsitlesime standardmudeli lahendamata küsimusi osakestefüüsikas ja kosmoloogias, sealhulgas tumeda aine olemust, inflatsiooni, vaakumi stabiilsust, neutriino massi tekkemehhanisme ning Higgsi bosoni massi võimalikku ebaloomulikku peenhäälestust. Viimase mainitud probleemi leevendamiseks uurisime klassikaliselt mastaabi-invariantsed mudeleid. Kuigi sellised mudelid on olnud teada juba üle 50 aasta, näitasime, et selles raamistikus leidub endiselt arenguruumi.

Esimeses publikatsioonis [111] arendasime uue meetodi tasase suuna kindlaks tegemiseks mastaabi-invariantsetes potentsiaalides. Näitasime, et biruut-potentsiaalide korral on tasase suuna olemasolul interaktsioonide maatriksi determinant null. Selle tulemusele tuginedes tuletasime lihtsa viisi Hesse maatriksi leidmiseks juhul, kui interaktsioonid ja eelistatud tasane suund on teada. Samuti leidsime lihtsa võrrandi interaktsioonitugevuste leidmiseks kui skalaarosakeste massid ja tasane suund on teada. Üldistasime saadud tulemuse ka üldistele neljanda astme potentsiaalidele, kasutades tensorite omaväärtuste formalismi, ning tõime välja konkreetsed näited: kahe- ja kolmeväljalised juhud biruut-potentsiaalide korral ning kaheväljalise näite üldise neljanda astme potentsiaali puhul. Pakutud uus lähenemine lihtsustab oluliselt keerukate skalaarsektorite analüüsi, võimaldades nende fenomenoloogilist uurimist märgatavalt tõhusamal kujul.

Teises publikatsioonis [116] uurisime klassikaliselt mastaabi-invariantset mudelit, mis sisaldas laiendatud skalaarsektorit kahe reaalsete kalibratsiooniteisenduste singletiga. Selles mudelis käsitlesime mitme faasiga kriitilisuse režiimi, kus kvantparandused, mida tavapärases Gildener–Weinbergi lähenduses on tühised, muutuvad oluliseks. Sellel piirjuhul ilmneb tugev seos

tumeaine ja Higgsi fenomenoloogia vahel, kuna interaktsioonid tumeainega määravad sümmeetria rikkumise dünaamika. Selle tulemusena on Higgsi bosoni mass väike, sest see tuleneb kvantparandustest sarnaselt dilatoniga. Näitasime, et mudelit saab kirjeldada kolme vaba parameetriga ning leidsime parameetrite piirkonna, mis on kooskõlas eksperimentaalsete piirangutega nagu tumeaine otsese detekteerimise tulemused ja Higgsi nähtamatu lagunemise laius, tagades seejuures õige tumeaine relikt-tiheduse kui ka teooria perturbatiivse käitumise. Lisaks uurisime interaktsioonide renormrühma jooksmist, et leida energia skaala, kus teooria püsib perturbatiivsena.

Kolmandas publikatsioonis [114] analüüsisime pöörd-kiigemehhanismiga mudelit mastaabi-invariantse potentsiaaliga, mis sisaldab lisaks Standardmudeli Higgsi dubletile üht kompleksset ja üht reaalset skalaarset singleti. Selles raamistikus omandab kompleksse singleti imaginaarne osa, majoron, massi leptonarvu otsese rikkumise tõttu potentsiaalis. Kasutasime esimese publikatsiooni tulemusi, et kindlaks määrata tasase suuna tingimused. Mudeli parameetrite ruumi uurimiseks kirjutasime koodi Markovi ahela Monte Carlo simulatsiooniks, rakendades seejuures nii eksperimentaalseid piiranguid nagu Higgsi signaalitugevust, selle nähtamatu lagunemislaiust ja õiget neutriinomasside spektrit, kui ka teoreetilisi piiranguid nagu perturbatiivsus ja vaakumi stabiilsus. Leidsime ka piirkonna, kus majoron täidab kõiki tingimusi tumeaine kandidaadina. Nimelt, saavutab õige tumeaine relikt-tiheduse ning püsib kosmoloogilistel ajaskaala jooksul stabiilsena. Viimane tingimus on täidetud ainult siis, kui dilatoni vaakumi keskväärtus on suur ning tumeaine interaktsioonid seevastu väiksed. See tähendas aga, et liiga väikeste interaktsioonide tõttu pole õige relikt-tiheduse saavutamine tavapärase väljakülmumise mehhanismiga võimalik. Seevastu sissekülmumise abil saavutasime vaatlusandmetega kooskõlalise tulemuse. Analüüsisime vastavas piirkonnas iseloomulikke interaktsioonitugevusi ning leidsime, et nii Standardmudeli Higgsi boson kui ka uus reaalne skalaarne singlett võivad sobida inflatoni rolli. Kuna Higgsi inflatsioon on kirjanduses juba põhjalikult käsitletud, keskendusime edasisel analüüsil uuele skalaarväljale. Näitasime, et uuritav mudel suudab üheaegselt kirjeldada nii neutriinode masse, tumedat ainet kui ka inflatsiooni, jäädes seejuures kooskõlla nii eksperimentaalsete kui ka teoreetiliste piirangutega.

Kõigi kolme publikatsiooni eesmärk oli täiendada klassikaliselt mastaabi-invariantsete mudelite käsitlust ja hinnata nende võimekust pakkuda lahendusi standardmudeli ning kosmoloogia senini lahendamata küsimustele, pöörates erilist tähelepanu tumeaine fenomenoloogiale.

Bibliography

[1] S. L. Glashow, J. Iliopoulos and L. Maiani, *Weak Interactions with Lepton-Hadron Symmetry*, *Phys. Rev. D* **2** (1970) 1285–1292.

[2] G. 't Hooft and M. J. G. Veltman, *Regularization and Renormalization of Gauge Fields*, *Nucl. Phys. B* **44** (1972) 189–213.

[3] D. J. Gross and F. Wilczek, *Ultraviolet Behavior of Nonabelian Gauge Theories*, *Phys. Rev. Lett.* **30** (1973) 1343–1346.

[4] CMS collaboration, S. Chatrchyan et al., *Observation of a New Boson at a Mass of 125 GeV with the CMS Experiment at the LHC*, *Phys. Lett. B* **716** (2012) 30–61, [1207.7235].

[5] ATLAS collaboration, G. Aad et al., *Observation of a new particle in the search for the Standard Model Higgs boson with the ATLAS detector at the LHC*, *Phys. Lett. B* **716** (2012) 1–29, [1207.7214].

[6] Super-Kamiokande collaboration, Y. Fukuda et al., *Evidence for oscillation of atmospheric neutrinos*, *Phys. Rev. Lett.* **81** (1998) 1562–1567, [hep-ex/9807003].

[7] IceCube collaboration, M. G. Aartsen et al., *The IceCube Neutrino Observatory: Instrumentation and Online Systems*, *JINST* **12** (2017) P03012, [1612.05093].

[8] RENO collaboration, J. K. Ahn et al., *Observation of Reactor Electron Antineutrino Disappearance in the RENO Experiment*, *Phys. Rev. Lett.* **108** (2012) 191802, [1204.0626].

[9] D. Buttazzo, G. Degrassi, P. P. Giardino, G. F. Giudice, F. Sala, A. Salvio et al., *Investigating the near-criticality of the Higgs boson*, *JHEP* **12** (2013) 089, [1307.3536].

[10] Supernova Cosmology Project collaboration, S. Perlmutter et al., *Measurements of Ω and Λ from 42 High Redshift Supernovae*, *Astrophys. J.* **517** (1999) 565–586, [astro-ph/9812133].

[11] M. Davis, G. Efstathiou, C. S. Frenk and S. D. M. White, *The Evolution of Large Scale Structure in a Universe Dominated by Cold Dark Matter*, *Astrophys. J.* **292** (1985) 371–394.

[12] M. Boylan-Kolchin, V. Springel, S. D. M. White, A. Jenkins and G. Lemson, *Resolving Cosmic Structure Formation with the Millennium-II Simulation*, *Mon. Not. Roy. Astron. Soc.* **398** (2009) 1150, [0903.3041].

[13] J. Wang, S. Bose, C. S. Frenk, L. Gao, A. Jenkins, V. Springel et al., *Universal structure of dark matter haloes over a mass range of 20 orders of magnitude*, *Nature* **585** (2020) 39–42, [1911.09720].

[14] V. C. Rubin and W. K. Ford, Jr., *Rotation of the Andromeda Nebula from a Spectroscopic Survey of Emission Regions*, *Astrophys. J.* **159** (1970) 379–403.

[15] F. Zwicky, *On the Masses of Nebulae and of Clusters of Nebulae*, *Astrophys. J.* **86** (1937) 217–246.

[16] Planck collaboration, N. Aghanim et al., *Planck 2018 results. VI. Cosmological parameters*, *Astron. Astrophys.* **641** (2020) A6, [1807.06209].

[17] A. A. Starobinsky, *A New Type of Isotropic Cosmological Models Without Singularity*, *Phys. Lett. B* **91** (1980) 99–102.

[18] A. H. Guth, *The Inflationary Universe: A Possible Solution to the Horizon and Flatness Problems*, *Phys. Rev. D* **23** (1981) 347–356.

[19] A. D. Linde, *A New Inflationary Universe Scenario: A Possible Solution of the Horizon, Flatness, Homogeneity, Isotropy and Primordial Monopole Problems*, *Phys. Lett. B* **108** (1982) 389–393.

[20] E. Gildener and S. Weinberg, *Symmetry Breaking and Scalar Bosons*, *Phys. Rev. D* **13** (1976) 3333.

[21] W. Heisenberg and W. Pauli, *On Quantum Field Theory. (In German)*, *Z. Phys.* **56** (1929) 1–61.

[22] S. Weinberg, *A Model of Leptons*, *Phys. Rev. Lett.* **19** (1967) 1264–1266.

[23] M. Gell-Mann, *A Schematic Model of Baryons and Mesons*, *Phys. Lett.* **8** (1964) 214–215.

[24] S. L. Glashow, *Partial Symmetries of Weak Interactions*, *Nucl. Phys.* **22** (1961) 579–588.

[25] A. Salam, *Weak and Electromagnetic Interactions*, *Conf. Proc. C* **680519** (1968) 367–377.

[26] C.-N. Yang and R. L. Mills, *Conservation of Isotopic Spin and Isotopic Gauge Invariance*, *Phys. Rev.* **96** (1954) 191–195.

[27] P. W. Higgs, *Broken Symmetries and the Masses of Gauge Bosons*, *Phys. Rev. Lett.* **13** (1964) 508–509.

[28] P. W. Higgs, *Spontaneous Symmetry Breakdown without Massless Bosons*, *Phys. Rev.* **145** (1966) 1156–1163.

[29] F. Englert and R. Brout, *Broken Symmetry and the Mass of Gauge Vector Mesons*, *Phys. Rev. Lett.* **13** (1964) 321–323.

[30] G. S. Guralnik, C. R. Hagen and T. W. B. Kibble, *Global Conservation Laws and Massless Particles*, *Phys. Rev. Lett.* **13** (1964) 585–587.

[31] T. W. B. Kibble, *Symmetry breaking in nonAbelian gauge theories*, *Phys. Rev.* **155** (1967) 1554–1561.

[32] J. Goldstone, A. Salam and S. Weinberg, *Broken Symmetries*, *Phys. Rev.* **127** (1962) 965–970.

[33] Particle Data Group collaboration, P. A. Zyla et al., *Review of Particle Physics*, *PTEP* **2020** (2020) 083C01.

[34] ATLAS collaboration, G. Aad et al., *Combined Measurement of the Higgs Boson Mass from the $H\to\gamma\gamma$ and $H\to ZZ^*\to 4\ell$ Decay Channels with the ATLAS Detector Using s=7, 8, and 13 TeV pp Collision Data*, *Phys. Rev. Lett.* **131** (2023) 251802, [2308.04775].

[35] W. A. Bardeen, *On naturalness in the standard model*, in *Ontake Summer Institute on Particle Physics*, 8, 1995.

[36] C. G. Callan, Jr., *Broken scale invariance in scalar field theory*, *Phys. Rev. D* **2** (1970) 1541–1547.

[37] K. Symanzik, *Small distance behavior in field theory and power counting*, *Commun. Math. Phys.* **18** (1970) 227–246.

[38] ATLAS, CMS collaboration, A. Hayrapetyan et al., *Combination of Measurements of the Top Quark Mass from Data Collected by the ATLAS and CMS Experiments at s=7 and 8 TeV*, *Phys. Rev. Lett.* **132** (2024) 261902, [2402.08713].

[39] S. R. Coleman, *The Fate of the False Vacuum. 1. Semiclassical Theory*, *Phys. Rev. D* **15** (1977) 2929–2936.

[40] E. A. Zaborowski et al., *A Sound Horizon-Free Measurement of H_0 in DESI 2024*, 2411.16677.

[41] G. Efstathiou and S. Gratton, *The evidence for a spatially flat Universe*, *Mon. Not. Roy. Astron. Soc.* **496** (2020) L91–L95, [2002.06892].

[42] A. Einstein, *The foundation of the general theory of relativity.*, *Annalen Phys.* **49** (1916) 769–822.

[43] G. Lemaitre, *A Homogeneous Universe of Constant Mass and Growing Radius Accounting for the Radial Velocity of Extragalactic Nebulae*, *Annales Soc. Sci. Bruxelles A* **47** (1927) 49–59.

[44] E. Hubble, *A relation between distance and radial velocity among extra-galactic nebulae*, *Proc. Nat. Acad. Sci.* **15** (1929) 168–173.

[45] J. Jørgensen, *Strong interactions for cosmology*, 2015.

[46] J. Ellis and D. Wands, *Inflation (2023)*, 2312.13238.

[47] S. D. Odintsov, V. K. Oikonomou, I. Giannakoudi, F. P. Fronimos and E. C. Lymperiadou, *Recent Advances in Inflation*, *Symmetry* **15** (2023) 1701, [2307.16308].

[48] J. de Haro and E. Elizalde, *Topics in Cosmology—Clearly Explained by Means of Simple Examples*, *Universe* **8** (2022) 166, [2201.06097].

[49] M. Cirelli, A. Strumia and J. Zupan, *Dark Matter*, 2406.01705.

[50] P. J. E. Peebles and B. Ratra, *The Cosmological Constant and Dark Energy*, *Rev. Mod. Phys.* **75** (2003) 559–606, [astro-ph/0207347].

[51] D. Clowe, M. Bradac, A. H. Gonzalez, M. Markevitch, S. W. Randall, C. Jones et al., *A direct empirical proof of the existence of dark matter*, *Astrophys. J. Lett.* **648** (2006) L109–L113, [astro-ph/0608407].

[52] H. Hildebrandt et al., *KiDS-450: Cosmological parameter constraints from tomographic weak gravitational lensing*, *Mon. Not. Roy. Astron. Soc.* **465** (2017) 1454, [1606.05338].

[53] DES collaboration, A. Amon et al., *Dark Energy Survey Year 3 results: Cosmology from cosmic shear and robustness to data calibration*, *Phys. Rev. D* **105** (2022) 023514, [2105.13543].

[54] J. Adamek, D. Daverio, R. Durrer and M. Kunz, *General relativity and cosmic structure formation*, *Nature Phys.* **12** (2016) 346–349, [1509.01699].

[55] S. W. Randall, M. Markevitch, D. Clowe, A. H. Gonzalez and M. Bradac, *Constraints on the Self-Interaction Cross-Section of Dark Matter from Numerical Simulations of the Merging Galaxy Cluster 1E 0657-56*, *Astrophys. J.* **679** (2008) 1173–1180, [0704.0261].

[56] D. Harvey, R. Massey, T. Kitching, A. Taylor and E. Tittley, *The non-gravitational interactions of dark matter in colliding galaxy clusters*, *Science* **347** (2015) 1462–1465, [1503.07675].

[57] M. Kawasaki, K. Kohri and T. Moroi, *Big-Bang nucleosynthesis and hadronic decay of long-lived massive particles*, *Phys. Rev. D* **71** (2005) 083502, [astro-ph/0408426].

[58] S. R. De Groot, *Relativistic Kinetic Theory. Principles and Applications.* 1980.

[59] G. Steigman and M. S. Turner, *Cosmological Constraints on the Properties of Weakly Interacting Massive Particles*, *Nucl. Phys. B* **253** (1985) 375–386.

[60] G. Arcadi, M. Dutra, P. Ghosh, M. Lindner, Y. Mambrini, M. Pierre et al., *The waning of the WIMP? A review of models, searches, and constraints*, *Eur. Phys. J. C* **78** (2018) 203, [1703.07364].

[61] N. Bernal, M. Heikinheimo, T. Tenkanen, K. Tuominen and V. Vaskonen, *The Dawn of FIMP Dark Matter: A Review of Models and Constraints*, *Int. J. Mod. Phys. A* **32** (2017) 1730023, [1706.07442].

[62] L. J. Hall, K. Jedamzik, J. March-Russell and S. M. West, *Freeze-In Production of FIMP Dark Matter*, *JHEP* **03** (2010) 080, [0911.1120].

[63] N. Bellomo, K. V. Berghaus and K. K. Boddy, *Impact of freeze-in on dark matter isocurvature*, *JCAP* **11** (2023) 024, [2210.15691].

[64] LZ collaboration, J. Aalbers et al., *Dark Matter Search Results from 4.2 Tonne-Years of Exposure of the LUX-ZEPLIN (LZ) Experiment*, *Phys. Rev. Lett.* **135** (2025) 011802, [2410.17036].

[65] PandaX-II collaboration, X. Cui et al., *Dark Matter Results From 54-Ton-Day Exposure of PandaX-II Experiment*, *Phys. Rev. Lett.* **119** (2017) 181302, [1708.06917].

[66] PandaX-4T collaboration, Y. Meng et al., *Dark Matter Search Results from the PandaX-4T Commissioning Run*, *Phys. Rev. Lett.* **127** (2021) 261802, [2107.13438].

[67] XENON collaboration, E. Aprile et al., *Dark Matter Search Results from a One Ton-Year Exposure of XENON1T*, *Phys. Rev. Lett.* **121** (2018) 111302, [1805.12562].

[68] XENON collaboration, E. Aprile et al., *First Dark Matter Search with Nuclear Recoils from the XENONnT Experiment*, *Phys. Rev. Lett.* **131** (2023) 041003, [2303.14729].

[69] LZ collaboration, J. Aalbers et al., *First Dark Matter Search Results from the LUX-ZEPLIN (LZ) Experiment*, *Phys. Rev. Lett.* **131** (2023) 041002, [2207.03764].

[70] Fermi-LAT collaboration, M. Ackermann et al., *Searching for Dark Matter Annihilation from Milky Way Dwarf Spheroidal Galaxies with Six Years of Fermi Large Area Telescope Data*, *Phys. Rev. Lett.* **115** (2015) 231301, [1503.02641].

[71] AMS collaboration, M. Aguilar et al., *Towards Understanding the Origin of Cosmic-Ray Positrons*, *Phys. Rev. Lett.* **122** (2019) 041102.

[72] IceCube collaboration, M. G. Aartsen et al., *Search for annihilating dark matter in the Sun with 3 years of IceCube data*, *Eur. Phys. J. C* **77** (2017) 146, [1612.05949].

[73] C. A. Argüelles, D. Delgado, A. Friedlander, A. Kheirandish, I. Safa, A. C. Vincent et al., *Dark matter decay to neutrinos*, *Phys. Rev. D* **108** (2023) 123021, [2210.01303].

[74] V. F. Mukhanov and G. V. Chibisov, *Quantum Fluctuations and a Nonsingular Universe*, *JETP Lett.* **33** (1981) 532–535.

[75] A. H. Guth and S. Y. Pi, *Fluctuations in the New Inflationary Universe*, *Phys. Rev. Lett.* **49** (1982) 1110–1113.

[76] M. S. Turner, E. J. Weinberg and L. M. Widrow, *Bubble nucleation in first order inflation and other cosmological phase transitions*, *Phys. Rev. D* **46** (1992) 2384–2403.

[77] A. De Felice and S. Tsujikawa, *f(R) theories*, *Living Rev. Rel.* **13** (2010) 3, [1002.4928].

[78] A. R. Liddle and S. M. Leach, *How long before the end of inflation were observable perturbations produced?*, *Phys. Rev. D* **68** (2003) 103503, [astro-ph/0305263].

[79] G. Germán, R. G. Quaglia and A. M. M. Colorado, *Model independent bounds for the number of e-folds during the evolution of the universe*, *JCAP* **03** (2023) 004, [2212.03730].

[80] A. R. Liddle, P. Parsons and J. D. Barrow, *Formalizing the slow roll approximation in inflation*, *Phys. Rev. D* **50** (1994) 7222–7232, [astro-ph/9408015].

[81] L. Dai, M. Kamionkowski and J. Wang, *Reheating constraints to inflationary models*, *Phys. Rev. Lett.* **113** (2014) 041302, [1404.6704].

[82] R. Allahverdi, R. Brandenberger, F.-Y. Cyr-Racine and A. Mazumdar, *Reheating in Inflationary Cosmology: Theory and Applications*, *Ann. Rev. Nucl. Part. Sci.* **60** (2010) 27–51, [1001.2600].

[83] ACT collaboration, E. Calabrese et al., *The Atacama Cosmology Telescope: DR6 Constraints on Extended Cosmological Models*, 2503.14454.

[84] BICEP, Keck collaboration, P. A. R. Ade et al., *Improved Constraints on Primordial Gravitational Waves using Planck, WMAP, and BICEP/Keck Observations through the 2018 Observing Season*, *Phys. Rev. Lett.* **127** (2021) 151301, [2110.00483].

[85] LiteBIRD collaboration, E. Allys et al., *Probing Cosmic Inflation with the LiteBIRD Cosmic Microwave Background Polarization Survey*, *PTEP* **2023** (2023) 042F01, [2202.02773].

[86] CMB-S4 collaboration, K. Abazajian et al., *Snowmass 2021 CMB-S4 White Paper*, 2203.08024.

[87] S. Weinberg, *Baryon and Lepton Nonconserving Processes*, *Phys. Rev. Lett.* **43** (1979) 1566–1570.

[88] C. Giunti and C. W. Kim, *Fundamentals of Neutrino Physics and Astrophysics*. 2007, 10.1093/acprof:oso/9780198508717.001.0001.

[89] Z. Maki, M. Nakagawa and S. Sakata, *Remarks on the unified model of elementary particles*, *Prog. Theor. Phys.* **28** (1962) 870–880.

[90] R. Davis, Jr., D. S. Harmer and K. C. Hoffman, *Search for neutrinos from the sun*, *Phys. Rev. Lett.* **20** (1968) 1205–1209.

[91] R. Davis, *A review of the Homestake solar neutrino experiment*, *Prog. Part. Nucl. Phys.* **32** (1994) 13–32.

[92] Borexino collaboration, G. Alimonti et al., *The Borexino detector at the Laboratori Nazionali del Gran Sasso*, *Nucl. Instrum. Meth. A* **600** (2009) 568–593, [0806.2400].

[93] Super-Kamiokande collaboration, Y. Fukuda et al., *The Super-Kamiokande detector*, *Nucl. Instrum. Meth. A* **501** (2003) 418–462.

[94] SNO collaboration, Q. R. Ahmad et al., *Direct evidence for neutrino flavor transformation from neutral current interactions in the Sudbury Neutrino Observatory*, *Phys. Rev. Lett.* **89** (2002) 011301, [nucl-ex/0204008].

[95] SNO collaboration, Q. R. Ahmad et al., *Measurement of day and night neutrino energy spectra at SNO and constraints on neutrino mixing parameters*, *Phys. Rev. Lett.* **89** (2002) 011302, [nucl-ex/0204009].

[96] T2K collaboration, K. Abe et al., *Indication of Electron Neutrino Appearance from an Accelerator-produced Off-axis Muon Neutrino Beam*, *Phys. Rev. Lett.* **107** (2011) 041801, [1106.2822].

[97] NOvA collaboration, P. Adamson et al., *Measurement of the neutrino mixing angle θ_{23} in NOvA*, *Phys. Rev. Lett.* **118** (2017) 151802, [1701.05891].

[98] KamLAND collaboration, K. Eguchi et al., *First results from KamLAND: Evidence for reactor anti-neutrino disappearance*, *Phys. Rev. Lett.* **90** (2003) 021802, [hep-ex/0212021].

[99] Daya Bay collaboration, F. P. An et al., *Observation of electron-antineutrino disappearance at Daya Bay*, *Phys. Rev. Lett.* **108** (2012) 171803, [1203.1669].

[100] P. F. de Salas, D. V. Forero, S. Gariazzo, P. Martínez-Miravé, O. Mena, C. A. Ternes et al., *2020 global reassessment of the neutrino oscillation picture*, *JHEP* **02** (2021) 071, [2006.11237].

[101] DESI collaboration, A. G. Adame et al., *DESI 2024 VI: cosmological constraints from the measurements of baryon acoustic oscillations*, *JCAP* **02** (2025) 021, [2404.03002].

[102] F. Bonnet, M. Hirsch, T. Ota and W. Winter, *Systematic study of the d=5 Weinberg operator at one-loop order*, *JHEP* **07** (2012) 153, [1204.5862].

[103] J. Schechter and J. W. F. Valle, *Neutrino Masses in SU(2) x U(1) Theories*, *Phys. Rev. D* **22** (1980) 2227.

[104] R. N. Mohapatra and G. Senjanovic, *Neutrino Mass and Spontaneous Parity Nonconservation*, *Phys. Rev. Lett.* **44** (1980) 912.

[105] T. P. Cheng and L.-F. Li, *Neutrino Masses, Mixings and Oscillations in SU(2) x U(1) Models of Electroweak Interactions*, *Phys. Rev. D* **22** (1980) 2860.

[106] M. Magg and C. Wetterich, *Neutrino Mass Problem and Gauge Hierarchy*, *Phys. Lett. B* **94** (1980) 61–64.

[107] R. Foot, H. Lew, X. G. He and G. C. Joshi, *Seesaw Neutrino Masses Induced by a Triplet of Leptons*, *Z. Phys. C* **44** (1989) 441.

[108] S. M. Boucenna, S. Morisi and J. W. F. Valle, *The low-scale approach to neutrino masses*, *Adv. High Energy Phys.* **2014** (2014) 831598, [1404.3751].

[109] J. Schechter and J. W. F. Valle, *Neutrino Decay and Spontaneous Violation of Lepton Number*, *Phys. Rev. D* **25** (1982) 774.

[110] S. R. Coleman and E. J. Weinberg, *Radiative Corrections as the Origin of Spontaneous Symmetry Breaking*, *Phys. Rev. D* **7** (1973) 1888–1910.

[111] K. Kannike, A. Kubarski and L. Marzola, *Geometry of Flat Directions in Scale-Invariant Potentials*, *Phys. Rev. D* **99** (2019) 115034, [1904.07867].

[112] K. Kannike, *Vacuum Stability Conditions From Copositivity Criteria*, *Eur. Phys. J. C* **72** (2012) 2093, [1205.3781].

[113] R. Cottle, G. Habetler and C. Lemke, *On classes of copositive matrices*, *Linear Algebra and its Applications* **3** (1970) 295.

[114] K. Kannike, A. Kubarski, L. Marzola and A. Racioppi, *Pseudo-Goldstone dark matter in a radiative inverse seesaw scenario*, *JHEP* **12** (2023) 166, [2306.07865].

[115] K. Kannike, L. Marzola, M. Raidal and A. Strumia, *Light Higgs boson from multi-phase criticality in dynamical symmetry breaking*, *Phys. Lett. B* **816** (2021) 136241, [2102.01084].

[116] K. Kannike, N. Koivunen, A. Kubarski, L. Marzola, M. Raidal, A. Strumia et al., *Dark matter-induced multi-phase dynamical symmetry breaking*, *Phys. Lett. B* **832** (2022) 137214, [2204.01744].

Publications

Curriculum Vitae

Name:	Aleksei Kubarski
Date and place of birth:	February 21, 1995, Kohtla-Järve, Estonia
Citizenship:	Estonian
Address:	National Institute of Chemical Physics and Biophysics, Rävala 10, Tallinn 10143, Estonia
E-mail:	aleksei.kubarski@ut.ee

Education

2021-2026	PhD, theoretical physics University of Tartu
2018-2021	MSc, physics, University of Tartu
2015-2018	BSc, physics, University of Tartu
2011-2014	Nõo Gymnasium

Elulookirjeldus

Nimi:	Aleksei Kubarski
Sünniaeg ja koht:	21. veebruar, 1995, Kohtla-Järve, Eesti
Kodakondsus:	Eesti
Aadress:	Keemilise ja Bioloogilise Füüsika Instituut, Rävala 10, Tallinn 10143, Eesti
E-post:	aleksei.kubarski@ut.ee

Haridus

2021-2026	PhD, teoreetiline füüsika, Tartu Ülikool
2018-2021	MSc füüsika, Tartu Ülikool
2015-2018	BSc, füüsika, Tartu Ülikool
2011-2014	Nõo Reaalgümnaasium

DISSERTATIONES PHYSICAE UNIVERSITATIS TARTUENSIS

1. **Andrus Ausmees**. XUV-induced electron emission and electron-phonon interaction in alkali halides. Tartu, 1991.
2. **Heiki Sõnajalg**. Shaping and recalling of light pulses by optical elements based on spectral hole burning. Tartu, 1991.
3. **Sergei Savihhin**. Ultrafast dynamics of F-centers and bound excitons from picosecond spectroscopy data. Tartu, 1991.
4. **Ergo Nõmmiste**. Leelishalogeniidide röntgenelektronemissioon kiiritamisel footonitega energiaga 70–140 eV. Tartu, 1991.
5. **Margus Rätsep**. Spectral gratings and their relaxation in some low-temperature impurity-doped glasses and crystals. Tartu, 1991.
6. **Tõnu Pullerits**. Primary energy transfer in photosynthesis. Model calculations. Tartu, 1991.
7. **Olev Saks**. Attoampri diapasoonis voolude mõõtmise füüsikalised alused. Tartu, 1991.
8. **Andres Virro**. AlGaAsSb/GaSb heterostructure injection lasers. Tartu, 1991.
9. **Hans Korge**. Investigation of negative point discharge in pure nitrogen at atmospheric pressure. Tartu, 1992.
10. **Jüri Maksimov**. Nonlinear generation of laser VUV radiation for high-resolution spectroscopy. Tartu, 1992.
11. **Mark Aizengendler**. Photostimulated transformation of aggregate defects and spectral hole burning in a neutron-irradiated sapphire. Tartu, 1992.
12. **Hele Siimon**. Atomic layer molecular beam epitaxy of A^2B^6 compounds described on the basis of kinetic equations model. Tartu, 1992.
13. **Tõnu Reinot**. The kinetics of polariton luminescence, energy transfer and relaxation in anthracene. Tartu, 1992.
14. **Toomas Rõõm**. Paramagnetic H^{2-} and F^+ centers in CaO crystals: spectra, relaxation and recombination luminescence. Tallinn, 1993.
15. **Erko Jalviste**. Laser spectroscopy of some jet-cooled organic molecules. Tartu, 1993.
16. **Alvo Aabloo**. Studies of crystalline celluloses using potential energy calculations. Tartu, 1994.
17. **Peeter Paris**. Initiation of corona pulses. Tartu, 1994.
18. **Павел Рубин**. Локальные дефектные состояния в CuO_2 плоскостях высокотемпературных сверхпроводников. Тарту, 1994.
19. **Olavi Ollikainen**. Applications of persistent spectral hole burning in ultrafast optical neural networks, time-resolved spectroscopy and holographic interferometry. Tartu, 1996.
20. **Ülo Mets**. Methodological aspects of fluorescence correlation spectroscopy. Tartu, 1996.
21. **Mikhail Danilkin**. Interaction of intrinsic and impurity defects in CaS:Eu luminophors. Tartu, 1997.

22. **Ирина Кудрявцева**. Создание и стабилизация дефектов в кристаллах KBr, KCl, RbCl при облучении ВУФ-радиацией. Тарту, 1997.
23. **Andres Osvet**. Photochromic properties of radiation-induced defects in diamond. Tartu, 1998.
24. **Jüri Örd**. Classical and quantum aspects of geodesic multiplication. Tartu, 1998.
25. **Priit Sarv**. High resolution solid-state NMR studies of zeolites. Tartu, 1998.
26. **Сергей Долгов**. Электронные возбуждения и дефектообразование в некоторых оксидах металлов. Тарту, 1998.
27. **Kaupo Kukli**. Atomic layer deposition of artificially structured dielectric materials. Tartu, 1999.
28. **Ivo Heinmaa**. Nuclear resonance studies of local structure in $RBa_2Cu_3O_{6+x}$ compounds. Tartu, 1999.
29. **Aleksander Shelkan**. Hole states in CuO_2 planes of high temperature superconducting materials. Tartu, 1999.
30. **Dmitri Nevedrov**. Nonlinear effects in quantum lattices. Tartu, 1999.
31. **Rein Ruus**. Collapse of 3d (4f) orbitals in 2p (3d) excited configurations and its effect on the x-ray and electron spectra. Tartu, 1999.
32. **Valter Zazubovich**. Local relaxation in incommensurate and glassy solids studied by Spectral Hole Burning. Tartu, 1999.
33. **Indrek Reimand**. Picosecond dynamics of optical excitations in GaAs and other excitonic systems. Tartu, 2000.
34. **Vladimir Babin**. Spectroscopy of exciton states in some halide macro- and nanocrystals. Tartu, 2001.
35. **Toomas Plank**. Positive corona at combined DC and AC voltage. Tartu, 2001.
36. **Kristjan Leiger**. Pressure-induced effects in inhomogeneous spectra of doped solids. Tartu, 2002.
37. **Helle Kaasik**. Nonperturbative theory of multiphonon vibrational relaxation and nonradiative transitions. Tartu, 2002.
38. **Tõnu Laas**. Propagation of waves in curved spacetimes. Tartu, 2002.
39. **Rünno Lõhmus**. Application of novel hybrid methods in SPM studies of nanostructural materials. Tartu, 2002.
40. **Kaido Reivelt**. Optical implementation of propagation-invariant pulsed free-space wave fields. Tartu, 2003.
41. **Heiki Kasemägi**. The effect of nanoparticle additives on lithium-ion mobility in a polymer electrolyte. Tartu, 2003.
42. **Villu Repän**. Low current mode of negative corona. Tartu, 2004.
43. **Алексей Котлов**. Оксианионные диэлектрические кристаллы: зонная структура и электронные возбуждения. Tartu, 2004.
44. **Jaak Talts**. Continuous non-invasive blood pressure measurement: comparative and methodological studies of the differential servo-oscillometric method. Tartu, 2004.
45. **Margus Saal**. Studies of pre-big bang and braneworld cosmology. Tartu, 2004.

46. **Eduard Gerškevitš**. Dose to bone marrow and leukaemia risk in external beam radiotherapy of prostate cancer. Tartu, 2005.
47. **Sergey Shchemelyov**. Sum-frequency generation and multiphoton ionization in xenon under excitation by conical laser beams. Tartu, 2006.
48. **Valter Kiisk**. Optical investigation of metal-oxide thin films. Tartu, 2006.
49. **Jaan Aarik**. Atomic layer deposition of titanium, zirconium and hafnium dioxides: growth mechanisms and properties of thin films. Tartu, 2007.
50. **Astrid Rekker**. Colored-noise-controlled anomalous transport and phase transitions in complex systems. Tartu, 2007.
51. **Andres Punning**. Electromechanical characterization of ionic polymer-metal composite sensing actuators. Tartu, 2007.
52. **Indrek Jõgi**. Conduction mechanisms in thin atomic layer deposited films containing TiO_2. Tartu, 2007.
53. **Aleksei Krasnikov**. Luminescence and defects creation processes in lead tungstate crystals. Tartu, 2007.
54. **Küllike Rägo**. Superconducting properties of MgB_2 in a scenario with intra- and interband pairing channels. Tartu, 2008.
55. **Els Heinsalu**. Normal and anomalously slow diffusion under external fields. Tartu, 2008.
56. **Kuno Kooser**. Soft x-ray induced radiative and nonradiative core-hole decay processes in thin films and solids. Tartu, 2008.
57. **Vadim Boltrushko**. Theory of vibronic transitions with strong nonlinear vibronic interaction in solids. Tartu, 2008.
58. **Andi Hektor**. Neutrino Physics beyond the Standard Model. Tartu, 2008.
59. **Raavo Josepson**. Photoinduced field-assisted electron emission into gases. Tartu, 2008.
60. **Martti Pärs**. Study of spontaneous and photoinduced processes in molecular solids using high-resolution optical spectroscopy. Tartu, 2008.
61. **Kristjan Kannike**. Implications of neutrino masses. Tartu, 2008.
62. **Vigen Issahhanjan**. Hole and interstitial centres in radiation-resistant MgO single crystals. Tartu, 2008.
63. **Veera Krasnenko**. Computational modeling of fluorescent proteins. Tartu, 2008.
64. **Mait Müntel**. Detection of doubly charged higgs boson in the CMS detector. Tartu, 2008.
65. **Kalle Kepler**. Optimisation of patient doses and image quality in diagnostic radiology. Tartu, 2009.
66. **Jüri Raud**. Study of negative glow and positive column regions of capillary HF discharge. Tartu, 2009.
67. **Sven Lange**. Spectroscopic and phase-stabilisation properties of pure and rare-earth ions activated ZrO_2 and HfO_2. Tartu, 2010.
68. **Aarne Kasikov**. Optical characterization of inhomogeneous thin films. Tartu, 2010.
69. **Heli Valtna-Lukner**. Superluminally propagating localized optical pulses. Tartu, 2010.

70. **Artjom Vargunin**. Stochastic and deterministic features of ordering in the systems with a phase transition. Tartu, 2010.
71. **Hannes Liivat**. Probing new physics in e+e− annihilations into heavy particles via spin orientation effects. Tartu, 2010.
72. **Tanel Mullari**. On the second order relativistic deviation equation and its applications. Tartu, 2010.
73. **Aleksandr Lissovski**. Pulsed high-pressure discharge in argon: spectroscopic diagnostics, modeling and development. Tartu, 2010.
74. **Aile Tamm**. Atomic layer deposition of high-permittivity insulators from cyclopentadienyl-based precursors. Tartu, 2010.
75. **Janek Uin**. Electrical separation for generating standard aerosols in a wide particle size range. Tartu, 2011.
76. **Svetlana Ganina**. Hajusandmetega ülesanded kui üks võimalus füüsikaõppe efektiivsuse tõstmiseks. Tartu, 2011
77. **Joel Kuusk**. Measurement of top-of-canopy spectral reflectance of forests for developing vegetation radiative transfer models. Tartu, 2011.
78. **Raul Rammula**. Atomic layer deposition of HfO_2 – nucleation, growth and structure development of thin films. Tartu, 2011.
79. **Сергей Наконечный**. Исследование электронно-дырочных и интерстициал-вакансионных процессов в монокристаллах MgO и LiF методами термоактивационной спектроскопии. Тарту, 2011.
80. **Niina Voropajeva**. Elementary excitations near the boundary of a strongly correlated crystal. Tartu, 2011.
81. **Martin Timusk**. Development and characterization of hybrid electro-optical materials. Tartu, 2012, 106 p.
82. **Merle Lust**. Assessment of dose components to Estonian population. Tartu, 2012, 84 p.
83. **Karl Kruusamäe**. Deformation-dependent electrode impedance of ionic electromechanically active polymers. Tartu, 2012, 128 p.
84. **Liis Rebane**. Measurement of the $W \to \tau\nu$ cross section and a search for a doubly charged Higgs boson decaying to τ-leptons with the CMS detector. Tartu, 2012, 156 p.
85. **Jevgeni Šablonin**. Processes of structural defect creation in pure and doped MgO and NaCl single crystals under condition of low or super high density of electronic excitations. Tartu, 2013, 145 p.
86. **Riho Vendt**. Combined method for establishment and dissemination of the international temperature scale. Tartu, 2013, 108 p.
87. **Peeter Piksarv**. Spatiotemporal characterization of diffractive and non-diffractive light pulses. Tartu, 2013, 156 p.
88. **Anna Šugai**. Creation of structural defects under superhigh-dense irradiation of wide-gap metal oxides. Tartu, 2013, 108 p.
89. **Ivar Kuusik**. Soft X-ray spectroscopy of insulators. Tartu, 2013, 113 p.
90. **Viktor Vabson**. Measurement uncertainty in Estonian Standard Laboratory for Mass. Tartu, 2013, 134 p.

91. **Kaupo Voormansik**. X-band synthetic aperture radar applications for environmental monitoring. Tartu, 2014, 117 p.
92. **Deivid Pugal**. hp-FEM model of IPMC deformation. Tartu, 2014, 143 p.
93. **Siim Pikker**. Modification in the emission and spectral shape of photo-stable fluorophores by nanometallic structures. Tartu, 2014, 98 p.
94. **Mihkel Pajusalu**. Localized Photosynthetic Excitons. Tartu, 2014, 183 p.
95. **Taavi Vaikjärv**. Consideration of non-adiabaticity of the Pseudo-Jahn-Teller effect: contribution of phonons. Tartu, 2014, 129 p.
96. **Martin Vilbaste**. Uncertainty sources and analysis methods in realizing SI units of air humidity in Estonia. Tartu, 2014, 111 p.
97. **Mihkel Rähn**. Experimental nanophotonics: single-photon sources- and nanofiber-related studies. Tartu, 2015, 107 p.
98. **Raul Laasner**. Excited state dynamics under high excitation densities in tungstates. Tartu, 2015, 125 p.
99. **Andris Slavinskis**. EST Cube-1 attitude determination. Tartu, 2015, 104 p.
100. **Karlis Zalite**. Radar Remote Sensing for Monitoring Forest Floods and Agricultural Grasslands. Tartu, 2016, 124 p.
101. **Kaarel Piip**. Development of LIBS for *in-situ* study of ITER relevant materials. Tartu, 2016, 93 p.
102. **Kadri Isakar**. ^{210}Pb in Estonian air: long term study of activity concentrations and origin of radioactive lead. Tartu, 2016, 107 p.
103. **Artur Tamm**. High entropy alloys: study of structural properties and irradiation response. Tartu, 2016, 115 p.
104. **Rasmus Talviste**. Atmospheric-pressure He plasma jet: effect of dielectric tube diameter. Tartu, 2016, 107 p.
105. **Andres Tiko**. Measurement of single top quark properties with the CMS detector. Tartu, 2016, 161 p.
106. **Aire Olesk**. Hemiboreal Forest Mapping with Interferometric Synthetic Aperture Radar. Tartu, 2016, 121 p.
107. **Fred Valk**. Nitrogen emission spectrum as a measure of electric field strength in low-temperature gas discharges. Tartu, 2016, 149 p.
108. **Manoop Chenchiliyan**. Nano-structural Constraints for the Picosecond Excitation Energy Migration and Trapping in Photosynthetic Membranes of Bacteria. Tartu, 2016, 115p.
109. **Lauri Kaldamäe**. Fermion mass and spin polarisation effects in top quark pair production and the decay of the higgs boson. Tartu, 2017, 104 p.
110. **Marek Oja**. Investigation of nano-size α- and transition alumina by means of VUV and cathodoluminescence spectroscopy. Tartu, 2017, 89 p.
111. **Viktoriia Levushkina**. Energy transfer processes in the solid solutions of complex oxides. Tartu, 2017, 101 p.
112. **Mikk Antsov**. Tribomechanical properties of individual 1D nanostructures: experimental measurements supported by finite element method simulations. Tartu, 2017, 101 p.
113. **Hardi Veermäe**. Dark matter with long range vector-mediated interactions. Tartu, 2017, 137 p.

114. **Aris Auzans**. Development of computational model for nuclear energy systems analysis: natural resources optimisation and radiological impact minimization. Tartu, 2018, 138 p.
115. **Aleksandr Gurev**. Coherent fluctuating nephelometry application in laboratory practice. Tartu, 2018, 150 p.
116. **Ardi Loot**. Enhanced spontaneous parametric downconversion in plasmonic and dielectric structures. Tartu, 2018, 164 p.
117. **Andreas Valdmann**. Generation and characterization of accelerating light pulses. Tartu, 2019, 85 p.
118. **Mikk Vahtrus**. Structure-dependent mechanical properties of individual one-dimensional metal-oxide nanostructures. Tartu, 2019, 110 p.
119. **Ott Vilson**. Transformation properties and invariants in scalar-tensor theories of gravity. Tartu, 2019, 183 p.
120. **Indrek Sünter**. Design and characterisation of subsystems and software for ESTCube-1 nanosatellite. Tartu, 2019, 195 p.
121. **Marko Eltermann**. Analysis of samarium doped TiO_2 optical and multi-response oxygen sensing capabilities. Tartu, 2019, 113 p.
122. **Kalev Erme**. The effect of catalysts in plasma oxidation of nitrogen oxides. Tartu, 2019, 114 p.
123. **Sergey Koshkarev**. A phenomenological feasibility study of the possible impact of the intrinsic heavy quark (charm) mechanism on the production of doubly heavy mesons and baryons. Tartu, 2020, 134 p.
124. **Kristi Uudeberg**. Optical Water Type Guided Approach to Estimate Water Quality in Inland and Coastal Waters. Tartu, 2020, 222 p.
125. **Daniel Blixt**. Hamiltonian analysis of covariant teleparallel theories of gravity. Tartu, 2021, 142 p.
126. **Ulbossyn Ualikhanova**. Gravity theories based on torsion: theoretical and observational constraints. Tartu, 2021, 154 p.
127. **Iaroslav Iakubivskyi**. Nanospacecraft for Technology Demonstration and Science Missions. Tartu, 2021, 177 p.
128. **Heido Trofimov**. Polluted clouds at air pollution hot spots help to better understand anthropogenic impacts on Earth's climate. Tartu, 2022, 96 p.
129. **Ott Rebane**. *In situ* non-contact sensing of microbiological contamination by fluorescence spectroscopy. Tartu, 2022, 157 p.
130. **Juhan Saaring**. Ultrafast Relaxation Processes in Ternary Hexafluorides Studied under Synchrotron Radiation Excitation. Tartu, 2022, 106 p.
131. **Ahmet Ilker Topuz**. Quantitative and qualitative investigations for muon scattering tomography via GEANT4 simulations: A computational study. Tartu, 2023, 163 p.
132. **Nico Benincasa**. Phase transitions and gravitational waves in models of dark matter. Tartu, 2023, 206 p.
133. **Kaja Pae**. Electron-phonon interactions in local degenerate electronic states in solids. Tartu, 2024, 201 p.
134. **Kristjan Müürsepp**. Phenomenological implications of Standard Model extensions. Tartu, 2024, 136 p.

135. **Ye Wang**. Investigating the properties of metal surfaces under high electric fields based on ab initio calculations. Tartu, 2024, 107 p.
136. **Laxmipriya Pati**. The effects of non-Riemannian connection in teleparallel gravity. Tartu, 2025, 172 p.
137. **Débora Aguiar Gomes**. Theoretical and astrophysical aspects of extended general relativity. Tartu, 2025, 169 p.
138. **Mina Hajizadeh Omaslanolya**. Structure and dynamics of photoactive proteins studied by (in situ-) neutron scattering methods. Tartu, 2025, 150 p.
139. **Aditya Savio Paul**. Advancing the study of small solar system bodies through multi-agent mapping and characterization. Tartu, 2025, 244 p.
140. **Sanu Bifal Maji**. Synthesis and luminescence investigation of nano-particles doped with Pr^{3+} ions in selected fluoride and phosphate hosts. Tartu, 2025, 114 p.
141. **Ernest Michael Priidik Gallagher**. On the internal gauge theory analogy to the Cartan Khronon theory of gravity. Tartu, 2026, 221 p.
142. **Maria Naeem**. First order electroweak radiative corrections to the decay of the polarised *W* boson. Tartu, 2026, 236 p.
143. **Konstantinos Pallikaris**. Novel black holes in Einstein gravity. Tartu, 2026, 133 p.